



Cite this: *EES Batteries*, 2025, **1**, 1481

Halide-based solid electrolytes: opportunities and challenges in the synergistic development of all-solid-state Li/Na batteries

Xiaohan Tang,^a Fei Xie,^{ID *a} Yaxiang Lu,^{ID a,b,c} Xiaohui Rong,^{a,b,d} Liquan Chen^{a,b,c,d} and Yong-Sheng Hu^{ID *a,b,c,d}

In the ever-evolving wave of energy storage technologies, all-solid-state batteries (ASSBs) have garnered significant attention due to their high energy density, long cycle life and intrinsic safety, being regarded as the necessary features of next-generation batteries. Halide-based solid electrolytes have emerged as promising candidates for next-generation ASSBs owing to their superior oxidative stability and tunable high ionic conductivity. This review aims to provide a comprehensive overview of the latest advances and state-of-the-art research progress in Li- and Na-based halide electrolytes. The common synthesis strategies, various categories of halide-based electrolytes, and their ion transport mechanisms are discussed in detail. Furthermore, various modification strategies for improving ionic conductivity, air stability and electrochemical stability are also discussed. Finally, we also offer insights into the current challenges and future perspectives of halide-based electrolytes. We anticipate that this review can serve as a guide for the design and understanding of halide-based electrolytes and promote their further advancement in the application of ASSBs toward energy storage.

Received 31st March 2025,
Accepted 27th July 2025

DOI: 10.1039/d5eb00064e

rsc.li/EESBatteries

Broader context

Against the background of rapidly advancing global energy storage technologies, all-solid-state batteries (ASSBs) have increasingly attracted widespread attention from both researchers and industry due to their unique advantages. As a crucial component of ASSBs, the properties of solid electrolytes play a significant role in their overall development. Halide-based electrolytes, an emerging class of solid electrolyte materials, have shown great potential in next-generation ASSB research because of their excellent ionic conductivity and strong compatibility with oxide cathodes. In this review, we provide a comprehensive overview of the development trends and technical challenges of Li-based and Na-based halide electrolytes. We place particular emphasis on common synthesis methods, various structural types, and their ion transport behaviors. This review also systematically summarizes a series of modification techniques aimed at enhancing the ionic conductivity, air stability, and electrochemical stability of halide-based electrolytes. Finally, this review analyzes the main challenges of halide-based electrolytes faced in practical applications and proposes potential strategies for future development to promote their widespread use in ASSBs.

1. Introduction

The rapid evolution of renewable energy systems and electrified transportation has intensified the demand for advanced energy storage technologies that combine high energy density, intrinsic

safety, and long-term stability. Conventional Li-ion batteries (LIBs), despite their commercial success, face inherent limitations due to their reliance on flammable organic liquid electrolytes.^{1,2} These electrolytes pose significant safety hazards, including leakage, thermal runaway, and combustion or even explosion under mechanical or thermal stress, which are exacerbated in high-energy applications such as electric vehicles (EVs) and grid-scale energy storage systems.^{3–6} Furthermore, the scarcity and uneven global distribution of Li and Co resources, coupled with the fluctuating costs, have spurred interest in alternative battery technologies, particularly Na-ion batteries (NIBs), which leverage Na's natural abundance and cost-effectiveness.^{7–11} However, NIBs also inherit the safety drawbacks from the liquid electrolytes, hindering their scalability for large deployments. All-solid-state batteries (ASSBs), which

^aKey Laboratory for Renewable Energy, Beijing Key Laboratory for New Energy Materials and Devices, Beijing National Laboratory for Condensed Matter Physics, Institute of Physics, Chinese Academy of Sciences, Beijing, 100190, China.

E-mail: fxie@iphy.ac.cn, yshu@iphy.ac.cn

^bCollege of Materials Science and Optoelectronics Technology, University of Chinese Academy of Sciences, Beijing, 100049, China

^cHuairou Division, Institute of Physics, Chinese Academy of Sciences, Beijing 101400, China

^dYangtze River Delta Physics Research Center Co. Ltd, Liyang, 213300, China



replace liquid electrolytes with their solid-state counterparts, have emerged as a transformative solution to these challenges. By eliminating the flammable components, ASSBs are able to inherently mitigate fire and explosion hazards while enabling the use of high-capacity metallic anodes (e.g., Li or Na), thereby significantly boosting the energy density.^{8,12–14} In addition, without the liquid electrolyte with fluidity, the bipolar configurations are feasible with solid electrolytes (SEs) to increase the voltage and energy density of the cells, and continuous interfacial side reactions can be effectively impeded during the charge/discharge processes, so that the cycling lifespan could be prolonged in ASSBs.¹⁵

Solid electrolytes (SEs), as a critical component of ASSBs, decisively influence the battery performance. To achieve satisfactory electrochemical performance in ASSBs, the prerequisite is the development of solid electrolytes with high ionic conductivities, high electronic resistivities, excellent chemical and electrochemical stability, excellent machinability, and favorable interfacial compatibility.^{16,17} As early as the 1980s, Na- β -Al₂O₃ was used as an electrolyte in high-temperature Na-S batteries and Na-Fe/NiCl₂ batteries.¹⁸ However, these batteries could only operate at temperatures >300 °C, which increased the operational costs and safety risks. Through years of efforts, various types of SEs have been developed to meet the requirements for ASSBs operating at lower temperatures (<80 °C). Nevertheless, they still face some shortcomings such as relatively low room-temperature ionic conductivity, narrow electrochemical stability windows, and poor electrode/electrolyte interfacial compatibility. Currently, the most prominent Na-ion solid electrolytes include oxide-, halide-, sulfide-, borohydride-, and polymer-based electrolytes (Fig. 1a).^{19–21} Oxide-based electrolytes (e.g., Na- β -Al₂O₃ and NASICON) can achieve room-temperature ionic conductivities $>10^{-3}$ S cm⁻¹. However, they require extremely high sintering temperatures (>1000 °C) to reduce grain boundary resistance and exhibit poor interfacial contact with electrodes due to their high mechanical rigidity.^{22,23} Sulfide-based electrolytes

possess relatively higher room-temperature ionic conductivities over 10^{-2} S cm⁻¹ and soft mechanical properties that enable cold-press densification.^{24,25} Nevertheless, their inherently narrow electrochemical stability windows restrict the choices of cathode materials. They are also unstable against Na metal anodes and sensitive to moisture, which can cause the release of toxic H₂S. Borohydride-based electrolytes, offering high ionic conductivities and superior reduction stability, are hindered by costly raw materials and complex synthesis.^{26–28} Polymer-based electrolytes are typically flexible, enabling good interfacial contact and electrode compatibility, but they face challenges such as low room-temperature ionic conductivities and narrow electrochemical windows.^{29,30}

Halide-based electrolytes have recently garnered significant attention due to the inherent chemical properties of halide anions, which enable high ionic conductivities, high oxidative stability (>4 V vs. Li⁺/Li or >4 V vs. Na⁺/Na), and good deformability.^{31,32} In fact, research on the conductivity of LiX and ternary Li-X-M halides dates back to as early as the 1930s.³³ However, their low ionic conductivities ($<10^{-5}$ S cm⁻¹) initially limited interest in halide-based electrolytes, causing research stagnation until 2018. In that year, Asano *et al.* synthesized Li₃YCl₆ and Li₃YBr₆ *via* ball milling and annealing, achieving room-temperature ionic conductivities of 0.51×10^{-3} S cm⁻¹ and 1.7×10^{-3} S cm⁻¹, respectively.³⁴ Since then, a series of novel halide superionic conductors have emerged, including water-mediated synthesis of Li₃InCl₆,³⁵ ball-milled and sintered Li₂ZrCl₆,³⁶ and Li-Ta-O-Cl,^{37,38} and viscoelastic-like LiAlCl_{2.5}O_{0.75}.³⁹ The best-reported room-temperature ionic conductivity reaches 10^{-2} S cm⁻¹, rivaling those of state-of-the-art sulfide electrolytes and liquid electrolytes.³⁸ Additionally, halides exhibit high voltage stability (>4 V vs. Li⁺/Li or >4 V vs. Na⁺/Na). However, most studied halide-based electrolytes are Li-ion systems, with only a few Na-ion examples such as Na₂ZrCl₆,⁴⁰ NaAlCl_{2.5}O_{0.75},³⁹ NaTaCl₆,⁴¹ Na_{3-x}M_{1-x}Zr_xCl₆ (M = Y, Er),^{42,43} and NaMCl₄O (M = Ta, Nb),⁴⁴ all of which underper-

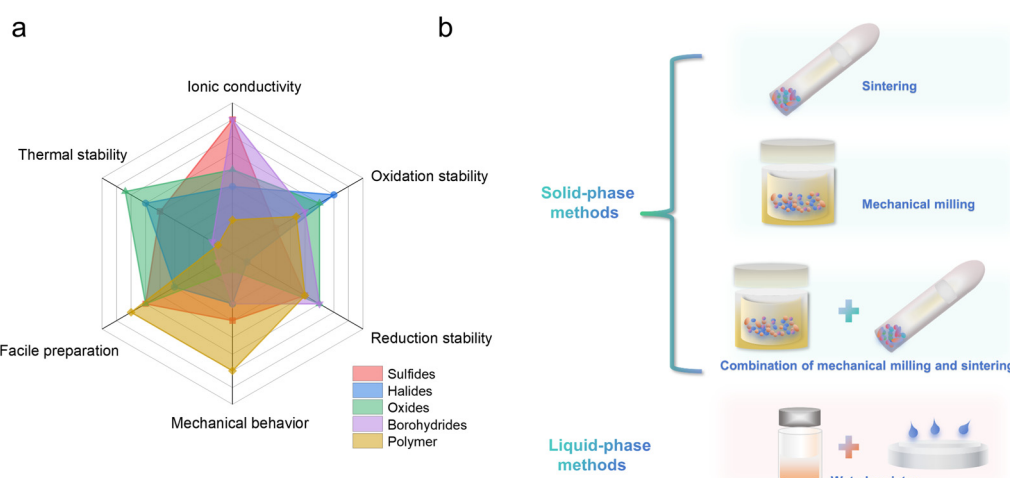


Fig. 1 (a) The radar chart compares the performance of key parameters of various solid-state electrolytes. (b) The schematic diagram of the solid-phase and liquid-phase methods of halide-based electrolytes.



form compared to their Li-based analogs. Despite their promising ionic conductivities and oxidative stability, practical applications of halide-based electrolytes remain hindered by challenges such as high raw material costs, complex synthesis steps, air sensitivity, and instability at the anode interface.

Current studies on halide-based electrolytes remain in their early stages, with a limited understanding of their ion transport mechanisms, interfacial compatibility with electrodes, and thermal/mechanical failure mechanisms. Additionally, there is significant room for improvement in ionic conductivities. In this review, we provide a comprehensive summary of the synthesis methods, categories, ion transport mechanisms, and chemical/electrochemical stabilities of Li/Na-based halide electrolytes. The outline of the structural design and modification strategies to enhance their performance are also discussed. Finally, we present insights into the current challenges and suggest future research perspectives for halide-based electrolytes.

2. Synthesis strategies

Synthesis strategies play a critical role in determining the properties of SE materials. Different processing routes and atmospheric conditions can significantly influence their structures, crystallinity, and ionic conductivities. Due to the air-sensitive and hygroscopic nature of the raw halide compounds, most synthesis procedures must be conducted under inert atmospheres (e.g., gloveboxes) or below the dew point to prevent moisture-induced degradation. Current synthesis methods for halide-based electrolytes primarily include solid-phase methods (mainly involving solid-phase sintering and mechanochemical protocols) and liquid-phase methods (water-mediated synthesis and ammonium-assisted synthesis), as shown in Fig. 1b.

Solid-phase synthesis is the most widely used method for preparing halide-based electrolytes. Early approaches involved sealing anhydrous raw materials into quartz tubes under vacuum or inert atmospheres for solid-state sintering. However, this method requires prolonged annealing times due to the sluggish reaction kinetics between solid compounds, although it can enhance the phase stability and crystallinity.^{45,46} Additionally, some binary halide mixtures exhibit low eutectic temperatures, enabling molten-state reactions during sintering, which can further shorten the processing durations.^{47,48}

Mechanochemical strategies represented by ball milling offer an alternative solid-phase route that can improve the homogeneity of the raw materials during the synthesis and reduce the reaction time. The mechanical energy generated during the milling provides the activation energy for the interactions among the precursors, yielding new materials distinct from the starting components. Unlike traditional sintering, high-energy ball milling produces disordered or locally distorted crystal structures and amorphous phases.^{49,50} These structural defects and amorphous domains can often enhance the ionic conductivity of the resulting halide-based electrolytes, in particular for the Na-based systems due to the larger ionic radius of Na^+ , so that the ionic transport is highly

impeded by some unsatisfied crystalline configurations and narrow bottlenecks. Notably, combining high-energy ball milling with subsequent annealing has also been reported, where the former can be used to improve the uniformity of raw material mixing and thus reduce the time of the solid-phase annealing reaction. For example, the annealing times were reduced to 1 h by introducing ball milling in advance in the preparation of Li_3ErCl_6 .⁵¹

Liquid-phase methods enable faster reaction kinetics, precise particle size control, and scalability for mass production. In 2019, Sun's group pioneered the aqueous synthesis of Li_3InCl_6 by dissolving LiCl and InCl_3 in water to form a hydrated intermediate ($\text{Li}_3\text{InCl}_6 \cdot x\text{H}_2\text{O}$), followed by vacuum heating.³⁵ The resulting Li_3InCl_6 achieved an ionic conductivity of $2.04 \times 10^{-3} \text{ S cm}^{-1}$, surpassing the values of the ones made using solid-phase methods. However, such aqueous approaches remain limited to specific systems because most halide-based electrolytes cannot reversibly transform between hydrated and anhydrous states.

Another liquid-phase route involves using organic solvents, but these are often complex and generate more pollutants. For example, Wang *et al.* developed an ammonium-assisted wet chemical method, introducing NH_4Cl to form intermediate $(\text{NH}_4)_3[\text{MCl}_6]$ complexes, and subsequent heat treatment produced halide electrolytes like Li_3YCl_6 .⁵² This method can successfully suppress the formation of M-O-Cl impurities during the pyrolysis process, and it can also be extended to some halide electrolytes with high conductivities such as Li_3ScCl_6 (1.25 mS cm^{-1}), Li_3ErCl_6 (0.41 mS cm^{-1}), and Li_3YBr_6 (1.08 mS cm^{-1}). Despite its versatility, this method releases corrosive gases (e.g., HCl , HBr) during ammonium salt decomposition, posing challenges for equipment durability and cost efficiency in large-scale production.

Currently, the synthesis of halide-based electrolytes is still primarily based on solid-phase methods, in particular the mechanochemical strategy, while the reports on liquid-phase methods are still relatively scarce. The selection of precursors and process parameters (such as the ball-milling reaction time, ball-to-material ratio, and the temperature, duration and atmosphere of sintering) plays a decisive role in the structure of halide-based electrolytes. For large-scale utilization of the halide-based electrolytes, it is still urgent to develop the synthesis methods that are low-cost, time-efficient, and easy to operate.

3. Structural type and diffusion mechanisms of halide-based electrolytes

Halide-based electrolytes are typically described by the chemical formula $\text{Li/Na}_a\text{MX}_b$ ($\text{M} = \text{metal element, X} = \text{F, Cl, Br, I}$). As M or X changes, it can lead to variations in the arrangement of anions and the occupancy of cation sites, thereby affecting the structure, ion transport mechanisms, and ionic conductivity of the halide-based electrolytes. In this manuscript, we classify



the halide-based electrolytes into three types (Fig. 2a and Table 1): the anionic frameworks (exemplified by the cubic close-packed sublattice in Li_3InCl_6), the cationic frameworks (UCl_3 -type), and amorphous.

3.1 Anionic frameworks (Li/Na-M-X , $\text{X} = \text{F, Cl, Br, I}$)

In the crystal structure of the anion framework-type halide electrolytes, the halide anions form a three-dimensional framework by sharing corners or edges with metal cations (such as Y^{3+} , In^{3+} , and Sc^{3+}) occupying octahedral or tetra-

hedral sites, while Li^+/Na^+ ions are distributed within the framework's interstices. In Li/Na-M-X compounds, the anions typically form a sublattice composed of a cubic close-packed (ccp) structure with an ABCABC stacking and a hexagonal close-packed (hcp) structure with an ABAB stacking (Fig. 2b).⁵³ However, the choice of metal cations, particularly their ionic radii, plays a decisive role in determining the crystal structure. Each close-packed structure can be further subdivided into crystal structures with different space groups, such as monoclinic ($\text{C}2/m$, $\text{P}2_1/n$) and cubic spinel ($\text{Fd}3\bar{m}$) structures for the

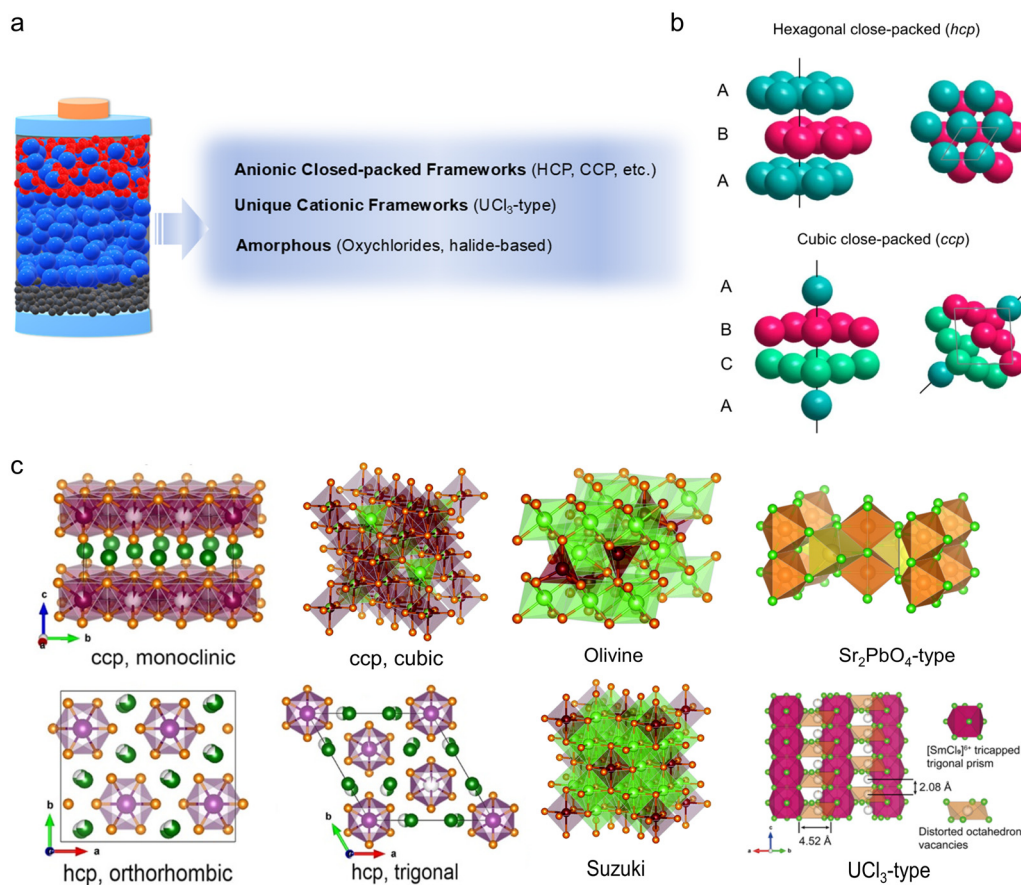


Fig. 2 (a) Classification of the existing halide-based electrolytes into three categories based on structural differences. (b) The cubic close-packed (ccp) structure and the hexagonal close-packed (hcp) structure.⁵³ (c) The crystal structure diagrams of the monoclinic, cubic, orthorhombic, trigonal, Suzuki, olivine, Sr_2PbO_4 - and UCl_3 -types.^{32,55,59,60}

Table 1 Types of halide-based electrolytes

	Crystal structure	Packing style	Representative electrolyte
Anionic frameworks	Monoclinic ($\text{C}2/m$, $\text{P}2_1/n$)	CCP	Li_3InCl_6 , Li_3ScCl_6 , Na_3YCl_6
	Cubic spinel ($\text{Fd}3\bar{m}$)	CCP	Li_2MCl_4 ($\text{M} = \text{Mg, Mn, Cd}$)
	Trigonal ($\text{P}3\bar{m}1$)	HCP	Li_3MCl_6 ($\text{M} = \text{Y, Tb-Tm}$), Na_2ZrCl_6 , Na_3InCl_6
	Orthorhombic (Pnma)	HCP	Li_3MCl_6 ($\text{M} = \text{Y, Ho-Lu}$)
	Olivine-type	—	High-temperature Li_2ZnCl_4 , Na_2ZnCl_4 , and Na_2CoCl_4
	Suzuki-type	—	Li_3MCl_8 , $\text{M} = \text{V, Fe, Co, Ni}$ and Li_6MnBr_8
	Sr_2PbO_4 -type	—	Na_2MgCl_4 , Na_2MnCl_4 , and Na_2CdCl_4
Cationic frameworks	UCl_3 -type	Non-close-packed	$\text{Na}_{3-x}\text{M}_{2-x}\text{Cl}_6$ ($\text{M} = \text{La-Sm}$) and NaM_2Cl_6 ($\text{M} = \text{Nd, Sm}$)
	Amorphous	—	Li/NaTaOCl_4 , Li/NaTaOCl_4 , $\text{LiAlCl}_{2.5}\text{O}_{0.75}$



ccp anion sublattice, as well as trigonal ($P\bar{3}m1$) and orthorhombic ($Pnma$) structures for the hcp anion sublattice (Fig. 2c). Moreover, in addition to these close-packed crystal configurations, other common structures that were formed for specific compounds include olivine-type (high-temperature Li_2ZnCl_4 , Na_2ZnCl_4 , and Na_2CoCl_4),^{54,55} Suzuki-type (Li_6MCl_8 , $M = V$, Fe , Co , Ni and Li_6MnBr_8),^{56,57} and Sr_2PbO_4 -type structures (Na_2MgCl_4 , Na_2MnCl_4 , and Na_2CdCl_4),⁵⁸ as shown in Fig. 2c.

Monoclinic halide electrolytes with a ccp anion sublattice in $Li-M-X$ electrolytes generally possess higher ionic conductivities and lower migration barriers. Currently, the octahedral sites of monoclinic $Li-M-X$ electrolytes are usually occupied by M^{3+} cations with an ionic radius less than 100 pm, mainly represented by Li_3InCl_6 ,³⁵ Li_3ScCl_6 ,⁶¹ and Li_3MBr_6 ($M = In$, Y , Sm - Lu)⁴⁵. Moreover, some researchers have computationally predicted that Li_3MI_6 ($M = Sc$, Y , La , etc.) could possess superionic conductor characteristics.⁶² However, in fact, only Li_3ErI_6 with an ionic conductivity of $0.65 \times 10^{-3} \text{ S cm}^{-1}$ has been successfully synthesized so far.⁶³ This is primarily due to the higher polarizability of I compared to Cl, which results in a softer lattice framework that is more conducive to Li^+ transport. In addition, Sun's and Wagemaker's groups both proposed the cation polarization factor and ionic potential, respectively, to guide the synthesis of monoclinic structures with high ionic conductivities (Fig. 3a and b).^{53,64} Nevertheless, there are still some exceptions such as the monoclinic Na_3YCl_6 with the $P2_1/n$ space group, which can be produced by slow cooling, but their ionic conductivity is extremely low ($10^{-6} \text{ S cm}^{-1}$ at 500 K).⁶⁵

Spinel-based halide electrolytes are also constructed from ccp, but they exhibit relatively low ionic conductivities at room temperature. As early as the 1980s to 1990s, Ryoji Kanno and H. D. Lutz, *et al.* systematically investigated spinels based on divalent metal cations (such as the first-row transition metals, Mg , Pb , etc.), where Li^+ ions have two different occupation sites in the structure.^{66,67} In the inverse spinel structure in Li_2MCl_4 ($M = Mg$, Mn , Cd), half of the Li occupy the corner-sharing tetrahedral sites, while the remaining Li occupy the octahedral sites together with the divalent metal cations.⁶⁸ Due to the favorable phase transition at high temperatures, the high-temperature phase can achieve an ionic conductivity of up to $10^{-2} \text{ S cm}^{-1}$. In the spinel structure of Li_2ZnCl_4 , all Li^+ ions reside in octahedral sites, while Zn^{2+} ions occupy the tetrahedral sites.⁵⁴ However, such an ion distribution hinders the Li^+ transportation, resulting in lower ionic conductivity. Moreover, Nazar's group synthesized a disordered spinel structure of $Li_2Sc_{2/3}Cl_4$ with a high ionic conductivity of $1.5 \times 10^{-3} \text{ S cm}^{-1}$.⁶⁹ Compared with Li_2MgCl_4 , the structure has four different sites of Li, and the disordered distribution of Li^+ in the tetrahedral and octahedral sites also forms a three-dimensional ion diffusion channel composed of face-sharing octahedra and tetrahedra, thereby achieving the high ionic conductivity (Fig. 3c).

The hcp close-packed structure of halide electrolytes is mainly composed of trigonal ($P\bar{3}m1$) and orthorhombic ($Pnma$)

phases. The metal cations in the trigonal phase have larger ionic radii than in the orthorhombic phase, but the ionic conductivity of the orthorhombic phase is usually one order of magnitude higher than that of the trigonal phase. Representative electrolytes of the trigonal phase with the $P\bar{3}m1$ space group include Li_3MCl_6 ($M = Y$, Tb - Tm),^{34,51,72,73} α - Li_2ZrCl_6 ,³⁶ Na_2ZrCl_6 ,⁴⁰ and Na_3InCl_6 ,⁷⁴ which have low room-temperature ionic conductivities, ranging from 10^{-5} to $10^{-4} \text{ S cm}^{-1}$. Li_3YCl_6 synthesized by Asano as a typical example of the trigonal phase has been widely studied.³⁴ In this structure, Y^{3+} , Li^+ , and vacancies occupy the octahedral sites in a molar ratio of $1:3:2$, and the existence of vacancies is the key to achieving an ionic conductivity of $10^{-4} \text{ S cm}^{-1}$. Furthermore, Mo's group calculated the theoretical room-temperature ionic conductivity of Li_3YCl_6 to be $1.4 \times 10^{-2} \text{ S cm}^{-1}$ through AIMD.⁷⁵ However, the experimental value is two orders of magnitude lower, primarily because of the similar ionic radii of Li^+ and Y^{3+} , which leads to their disordered distribution at the octahedral sites to form antioccupied defects, thus causing the block of Li^+ transport. The impurities and grain boundaries during synthesis also affect the conductivity. Based on theoretical calculations, Sokseihha Muy and colleagues predicted and successfully synthesized Li_3ErCl_6 *via* ball-milling, which is isostructural with Li_3YCl_6 , but the ionic conductivity was decreased after sintering from $0.3 \times 10^{-3} \text{ S cm}^{-1}$ to $0.05 \times 10^{-3} \text{ S cm}^{-1}$.⁵¹ Na_2ZrCl_6 synthesized *via* ball milling shows an ionic conductivity of $1.8 \times 10^{-5} \text{ S cm}^{-1}$, which also decreases after heating treatment since the crystallinity is enhanced.⁴⁰ The highly crystalline phase attributed to the strong bonding between Na and Cl in the lattice decreases the ionic conductivity. The orthorhombic structures with the $Pnma$ space group include Li_3MCl_6 ($M = Y$, Ho - Lu), and they can deliver the room-temperature ionic conductivities ranging from 0.32 to $1.3 \times 10^{-3} \text{ S cm}^{-1}$. Sun's group found that in the ternary chloride solid electrolytes, $Li_{3-3x}M_{1+x}Cl_6$ ($-0.14 < x \leq 0.5$, $M = Tb$, Dy , Ho , Y , Er , Tm) is beneficial for the structural transformation from the trigonal to the orthorhombic phase and significantly enhances the ionic conductivity as the x value increases (Fig. 3d).⁷⁰ Among them, the ionic conductivity of the orthorhombic phase $Li_{2.73}Ho_{1.09}Cl_6$ reaches as high as $1.3 \times 10^{-3} \text{ S cm}^{-1}$, around four times higher than that of the trigonal phase. This improvement is attributed to the formation of the orthorhombic phase, which makes it easier for Li^+ transport along the c -axis.

Halide electrolytes exhibit different anion packing arrangements, which also lead to variations in Li^+ transport pathways and dynamics. In ccp anion sublattices, Li^+ ions typically occupy octahedral and tetrahedral sites, allowing migration along the crystal planes and interstitial sites in multiple directions. These interconnected pathways form a complex but highly efficient three-dimensional transport network, and the diffusion is isotropic, which facilitates rapid ion migration. Li^+ ions usually jump from one octahedral site, pass through a tetrahedral site, and finally reach an adjacent octahedral site, namely Oct1-[Tet1 or Tet2]-Oct2 and Oct1Tet3-Oct3 (Fig. 3e). In contrast, the diffusion of Li^+ in the hcp anion sublattice is



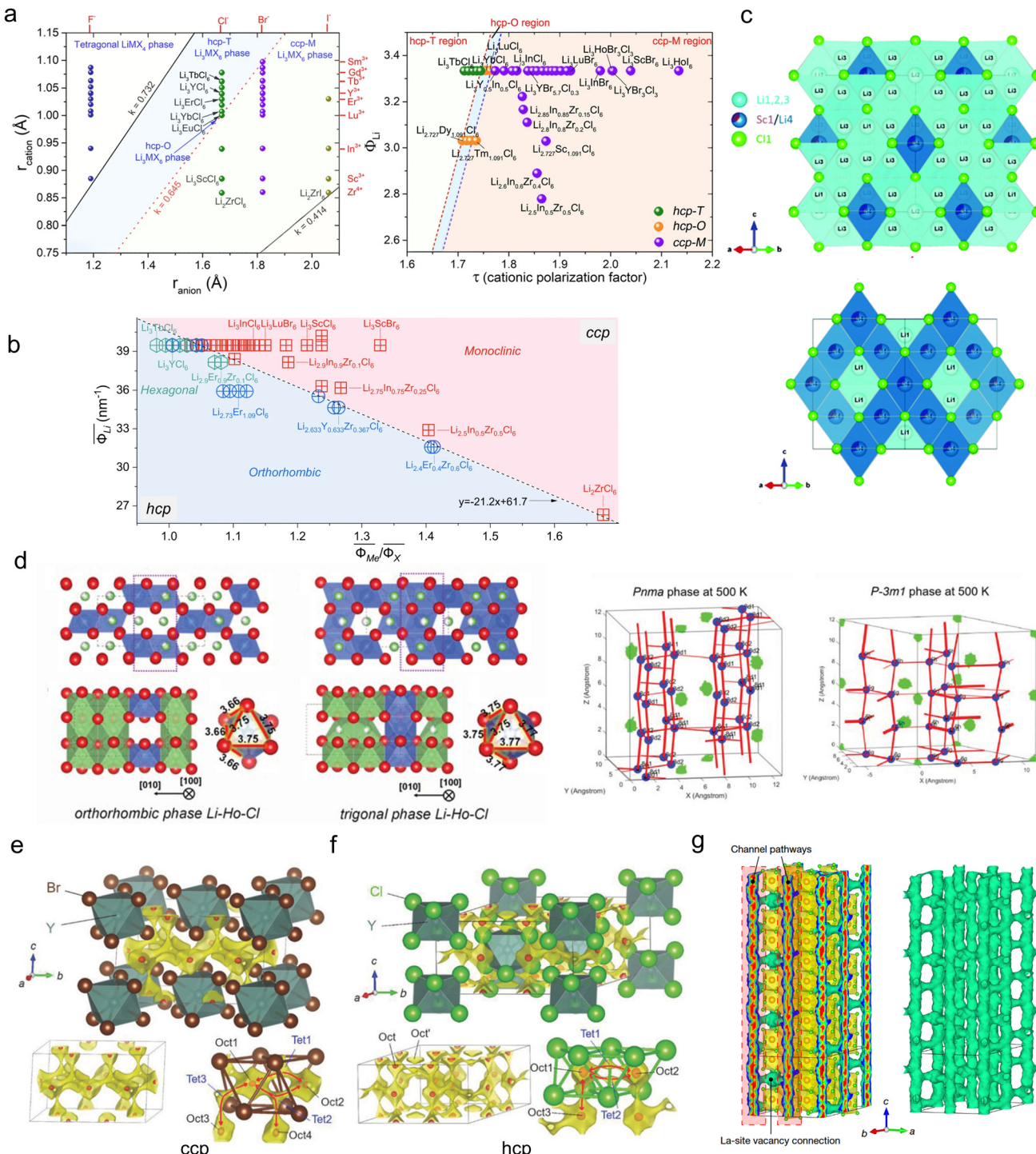


Fig. 3 The phase map showing representative halide-based electrolytes as a function of (a) cation polarization factor⁶⁴ and (b) ionic potential⁵³ to guide the synthesis of monoclinic structures with high ionic conductivities. (c) The disordered spinel structure of $\text{Li}_3\text{Sc}_{2/3}\text{Cl}_4$.⁶⁹ (d) The orthorhombic and trigonal structures of Li_3HoCl_6 , and the ionic jumps between different Li^+ sites.⁷⁰ Crystal structures and Li^+ migration paths of (e) Li_3YCl_6 and (f) Li_3YBr_6 .³⁴ (g) The 3D Li^+ migration pathways of UCl_3 -type $\text{Li}_{0.388}\text{Ta}_{0.238}\text{La}_{0.475}\text{Cl}_3$.⁷¹

anisotropic. In the ab plane, Li^+ ions mainly migrate via tetrahedral sites (Oct1-[Tet1 or Tet2]-Oct2), while along the c -axis, they diffuse through octahedral sites (Oct1-Oct3), as shown in Fig. 3f.

3.2 Cationic frameworks (UCl_3 -type)

The UCl_3 -type superionic conductors have attracted significant attention due to their unique cationic framework and large ion

transport channels. Their structure is based on the lattice of lanthanum chloride LnCl_3 ($\text{Ln} = \text{La, Ce, Sm, Nd, etc.}$), which is composed of nine-coordinated $[\text{LnCl}_9]^{6-}$ polyhedra (Fig. 2c). The Cl^- ions are arranged in a non-close-packed anion framework forming larger one-dimensional diffusion channels. Owing to the large radius of Ln^{3+} (ranging from 124.7 pm to 135.6 pm) and the non-close-packed structure, the diffusion channels and coordination distortions are significantly larger than those in the traditional close-packed structure of Li/Na-M-X . However, the existing one-dimensional channels in the lattice are easily affected by blocking effects, leading to the lower ion diffusivity. To address this, Yao and colleagues first introduced Ta^{5+} doping to create La vacancies and construct three-dimensional ion transport pathways (Fig. 3g).⁷¹ The synthesized $\text{Li}_{0.388}\text{Ta}_{0.238}\text{La}_{0.475}\text{Cl}_3$ achieved a high ionic conductivity of $3.02 \times 10^{-3} \text{ S cm}^{-1}$ at room temperature and exhibited excellent stability against metallic lithium anodes due to the low electronegativity of lanthanide elements. Additionally, Sun *et al.* reported a zeolite-like SmCl_3 framework structure.⁶⁰ The ionic conductivities of ball-milled (BM) electrolytes like BM- SmCl_3 -0.5LiCl and BM- SmCl_3 -0.5Li₂ZrCl₆ were $1.2 \times 10^{-4} \text{ S cm}^{-1}$ and $1.0 \times 10^{-3} \text{ S cm}^{-1}$, respectively. In fact, as early as in 1994, Meyer reported Na-based UCl₃-type compounds $\text{Na}_{3x}\text{M}_{2-x}\text{Cl}_6$ ($\text{M} = \text{La-Sm}$) and NaM_2Cl_6 ($\text{M} = \text{Nd, Sm}$), although their ionic conductivities were much lower than $10^{-4} \text{ S cm}^{-1}$.⁷⁶ Recently, Xiang *et al.* synthesized $\text{Na}_{0.7}\text{La}_{0.7}\text{Zr}_{0.3}\text{Cl}_4$ with an ionic conductivity of $2.9 \times 10^{-4} \text{ S cm}^{-1}$.⁷⁷ The moderate ionic conductivity was attributed to the doping of Zr^{4+} at the La^{3+} sites, which shortens the lengths of the Zr-Cl and La-Cl bonds, expanding the Na^+ diffusion pathways and improving the ionic conductivity. However, due to the anti-site defects between La and Na, a small fraction of La^{3+} in the one-dimensional diffusion pathways hinders the Na^+ transport and ultimately reduced the ionic conductivity. Furthermore, Sun's group developed a novel halide heterostructure by combining the high-coordination UCl₃-type framework ($\text{Na}_{0.75}\text{M}_{1.75}\text{Cl}_6$, $\text{M} = \text{La, Sm}$) with the Ta-based low-coordination amorphous halide electrolyte (NaTaCl_6).⁷⁸ The synthesized 0.62 $[\text{Na}_{0.75}\text{Sm}_{1.75}\text{Cl}_6]\text{-}0.38[\text{NaTaCl}_6]$ and 0.57 $[\text{Na}_{0.75}\text{La}_{1.75}\text{Cl}_6]\text{-}0.43[\text{NaTaCl}_6]$ exhibited high ionic conductivities of 2.7 mS cm^{-1} and 1.8 mS cm^{-1} , respectively. The amorphous regions are conducive to connecting discrete UCl₃-type particles, enabling long-range Na^+ diffusion and improved ionic conductivity. Currently, the development of UCl₃-type electrolytes, which have more promising opportunities for further research, remains limited.

3.3 Amorphous halide electrolytes

Among halide-based electrolytes, Li-based materials are still predominantly crystalline and some amorphous electrolytes with high ionic conductivity have also emerged, whereas Na-based electrolytes are mainly in the amorphous state. Amorphous halide-based electrolytes offer many advantages such as abundant intrinsic defects, few grain boundaries, and large transport spaces. However, due to the lack of long-range order in the structure, it is currently difficult to clearly explore their accurate ion transport mechanisms, and the study in this area is still in the early stage. The main representatives of

amorphous compounds include Li/NaTaCl_6 ,^{41,79} Li/NaTaOCl_4 ,^{37,80} and clay-like systems such as 2LiCl-GaF_3 and $\text{LiCl-AlF}_3\text{-GaF}_3$.⁸¹ Yao *et al.* successfully synthesized amorphous Li-Ta/Nb-Cl-based and composite electrolytes with various lithium salts such as LiF, Li₂O, LiOH, and Li₂O₂ *via* ball milling.⁷⁹ The room-temperature ionic conductivity can reach up to $7 \times 10^{-3} \text{ S cm}^{-1}$, which is mainly due to the inherent properties of the amorphous structure and the efficient Li^+ transport at the interfaces with LiCl particles. In the amorphous matrix, an appropriate amount of LiCl can release mobile Li^+ to promote conduction, whereas an excess of LiCl may impede the process. Similarly, NaCl and TaCl₅ can also be used to synthesize amorphous NaTaCl₆ with a high ionic conductivity ($4 \times 10^{-3} \text{ S cm}^{-1}$) through long-term ball milling.⁴¹ This is mainly due to the weakening of Na-Cl interactions, while the high-energy ball milling deforms the TaCl₆ octahedron and forms a poly-TaCl₆ framework, which repels Na^+ ions from entering the amorphous matrix and promotes their rapid migration (Fig. 4a). In addition, a new type of clay-like electrolyte material $x\text{LiCl-GaF}_3$ with a high ionic conductivity was reported with amorphous structures, which is attributed to $\text{Ga}(\text{F},\text{X})_n$ polyanions that weaken the Li-X interactions through charge aggregation and thereby promote the Li^+ transport (Fig. 4b).^{82,83} However, only the Li-Ga-F-Cl and analogous Mg-Ga-F-Cl systems have been successfully obtained as the clay-like lithium and magnesium conductors, respectively.⁸⁴ The formation principles of the clay-like properties and the corresponding clay-like electrolytes for Na-based batteries or those based on other precursors in addition to GaF₃ still require further exploration.

4 Modification strategies of halide-based electrolytes towards higher ionic conductivities

Although halide-based electrolytes have achieved remarkable progress over the past few years, ionic conductivity is still a key factor hindering their widespread application in ASSBs. Currently, only a few halide-based electrolytes can reach ionic conductivities exceeding $10^{-3} \text{ S cm}^{-1}$. To promote their practical application in ASSBs, it is essential to explore and implement effective strategies to further enhance their ionic conductivity. The common strategies mainly involve substituting anions/cations with different radii or valences, amorphization, and increasing the configuration entropies, which can effectively regulate the sublattice structures, charge carriers, and defect concentrations of the halide-based electrolytes, thereby optimizing ion diffusion and improving the ionic conductivity.

4.1 Cation modification

Cation modification is primarily achieved by introducing isovalent or aliovalent cations into the pristine frameworks. According to the differences in ionic radius and chemical

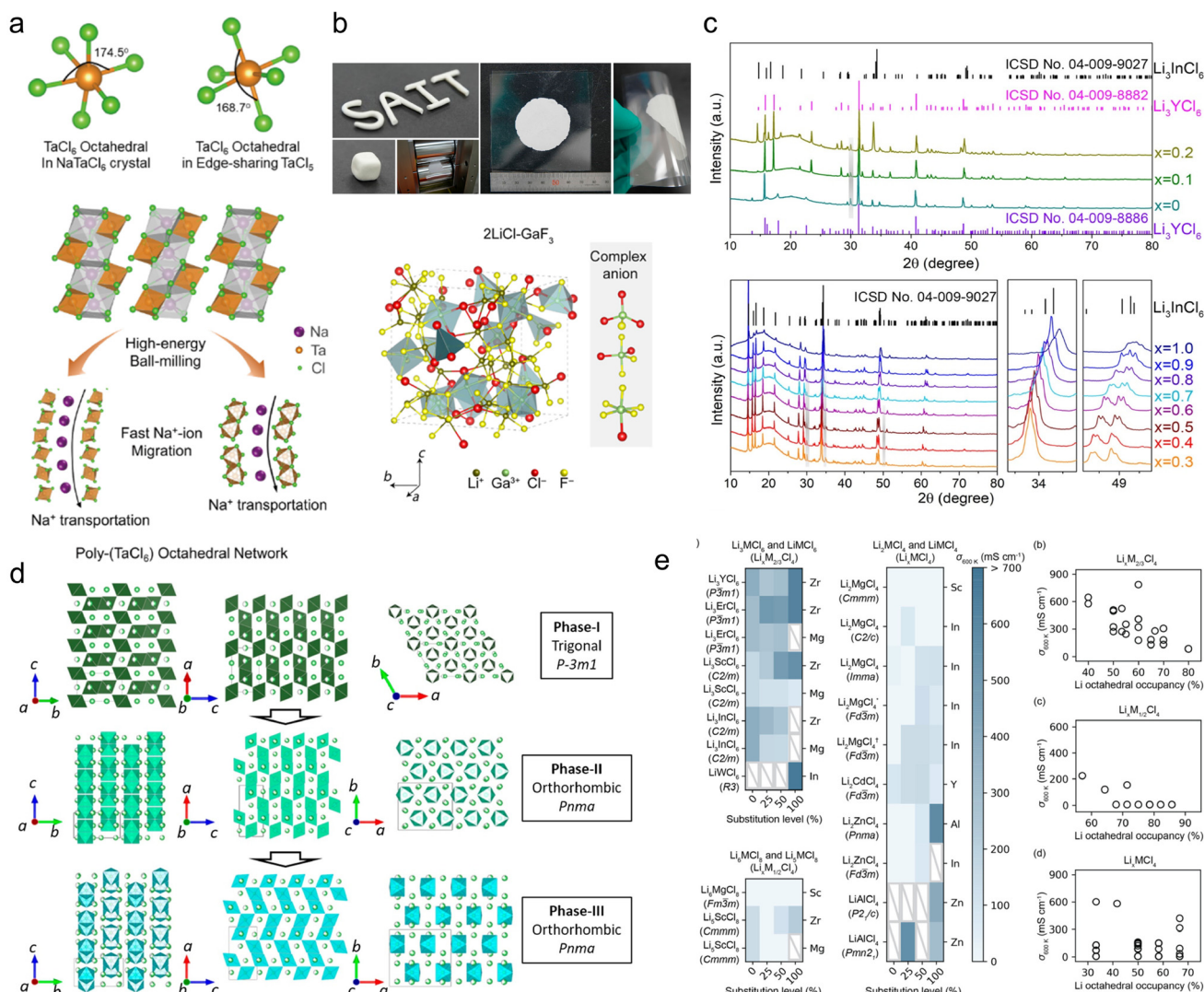


Fig. 4 (a) The Na^+ conduction mechanism and local structural distortion in NaTaCl_6 .⁴¹ (b) The clay-like amorphous electrolyte $x\text{LiCl}-\text{GaF}_3$.^{82,83} (c) By partially substituting In^{3+} , $\text{Li}_3\text{Y}_{1-x}\text{In}_x\text{Cl}_6$ can transition from the cubic phase to the trigonal phase.⁵⁹ (d) $\text{Li}_{3-x}\text{M}_{1-x}\text{Zr}_x\text{Cl}_6$ (M = Y, Er) with different amounts of Zr doping will result in phase transition.⁸⁵ (e) Effects on conductivity by tailoring the cation lattice and Li-content by high-throughput computational analysis.⁸⁶

bond characteristics among isovalent cations, isovalent substitution can alter the crystal structure and optimize the sublattice configuration to improve ion transport pathways and thereby increase the ionic conductivity. Ciucci and co-workers used density functional theory (DFT) to investigate the effects of metal cations with different ionic radii (M = Sr, Sc, La, Zr) on partial substitution in Li_3YCl_6 .⁸⁷ It was found that the partial substitution of Y by a larger cation such as La can enlarge the diffusion channels and lower the activation energy. In addition, the ionic conductivity can be improved by changing the doping level of isovalent cations, which can induce crystal structure transformations that enhance ionic conductivity. For example, by introducing partial In^{3+} into Li_3YCl_6 , the crystal structure of $\text{Li}_3\text{Y}_{1-x}\text{In}_x\text{Cl}_6$ ($0 < x < 1$) can change from the hcp-cubic phase to the hcp-trigonal phase (Fig. 4c).⁵⁹

When x exceeds 0.2, it can transform into the CCP-monoclinic phase with the ionic conductivity increased to $10^{-3} \text{ S cm}^{-1}$, indicating that the conversion of the sublattice plays a key role in promoting Li^+ transport. Isovalent cation substitution can also increase the vacancy concentration, allowing ions to hop more easily between these vacancies for rapid conduction. In the $\text{Li}_2\text{In}_{x}\text{Sc}_{0.666-x}\text{Cl}_4$, the In doping significantly enhanced ionic conductivity, reaching up to $2.03 \times 10^{-3} \text{ S cm}^{-1}$.⁸⁸ This is attributable to the increased disorder of Li^+ distribution and the additional vacancies generated that facilitate Li^+ migration. Although the overall crystal structures remain almost unchanged after doping, the alteration in Li occupancy forms a three-dimensional transport network that not only enhances the ionic conduction but also reduces the electronic conduction.



In addition to isovalent doping, aliovalent doping can also enhance ionic conductivity by altering carrier concentration/distribution, defect concentration, and local structures. Two common approaches include substituting low-valence metal cations with high-valence metal cations (Ta^{5+} , Nb^{5+} , Hf^{4+} , Zr^{4+} , etc.) to increase vacancy concentration or substituting high-valence metal cations with low-valence ones (Fe^{3+} , In^{3+} , etc.) to increase carrier concentration and promote ion transport. A widely studied system involves using the cost-effective Zr^{4+} to replace trivalent metal cations, forming $Li_{3-x}M_{1-x}Zr_xCl_6$ ($M = Y, Er$; $x = 0-0.6$).⁸⁵ The ionic conductivity can reach up to $1.4 \times 10^{-3} \text{ S cm}^{-1}$ compared to $10^{-5} \text{ S cm}^{-1}$ for pristine Li_3YCl_6 . The substitution induces a structural transformation from trigonal to orthorhombic, and the improvement in ionic conductivity is attributed to the vacancies introduced by Zr doping, which facilitates a three-dimensional transport network (Fig. 4d). Additionally, the introduction of extra tetrahedral Li sites is able to construct a more favorable Li^+ transport framework. Similarly, a solid solution of $Li_3In_{1-x}Zr_xCl_6$ is formed by the substitution of In^{3+} with Zr^{4+} .⁸⁹ This substitution not only generates additional lithium tetrahedral sites and vacancies but also induces cation disorder and local structural distortions, promoting the formation of a three-dimensional Li^+ transport pathway. This significantly increases the ionic conductivity to $1.25 \times 10^{-3} \text{ S cm}^{-1}$. Another example is the replacement of Yb^{3+} with Hf^{4+} in Li_3YbCl_6 , which results in a structural transformation from the orthorhombic phase to the monoclinic phase, which is favorable for Li^+ diffusion.⁹⁰

Furthermore, Mo and colleagues used high-throughput computational analysis to verify the ionic conduction in various aliovalent element-substituted chloride-based electrolytes (Fig. 4e).⁸⁶ Their study revealed the influence of Li content and cation sublattice on Li^+ conduction. They proposed that reducing lithium octahedral occupancy to 40%–60%, lowering the cation concentration, and increasing cation spacing to achieve a sparse cation distribution could further enhance Li^+ conductivity. The high-valence cation substitution approach is also applicable to Na-based halide electrolytes. For example, substituting Y^{3+} or Er^{3+} with Zr^{4+} in $Na_{2.125}Y_{0.125}Zr_{0.875}Cl_6$ and $Na_{2.4}Er_{0.4}Zr_{0.6}Cl_6$ can significantly improve the ionic conductivity, although the values still remained around $10^{-5} \text{ S cm}^{-1}$.^{42,43} The enhancement is mainly attributed to the increased vacancy concentration and the cooperative effect of multi-anion rotation with Na^+ . Additionally, Fu *et al.* synthesized a UCl_3 -type $Na_{1-x}La_{1-x}Zr_xCl_4$ electrolyte by replacing La^{3+} with Zr^{4+} , achieving an ionic conductivity of $2.9 \times 10^{-4} \text{ S cm}^{-1}$.⁷⁷ This improvement was primarily because Zr doping shortens the M–Cl bond length, expands the one-dimensional diffusion channel, and lowers the migration energy barrier, thereby enhancing the ionic conductivity. However, the presence of a small amount of La in the diffusion channel due to anti-site occupation with Na may hinder Na^+ diffusion. On the other hand, using low-valence cations such as Fe^{3+} , In^{3+} , and Sc^{3+} to replace the high-valence Zr^{4+} in $Li_{2+x}Zr_{1-x}M_xCl_6$ ($M = In, Sc, Fe$) resulted in electrolyte materials with high ionic conductivities ($>10^{-3} \text{ S cm}^{-1}$).^{91,92}

This enhancement is attributed to the increased Li^+ concentration and the expansion of the lattice volume caused by the dopants.

4.2 Anion modification

Similar to cation substitution, both isovalent and aliovalent anion substitution can alter the structure and even induce amorphous phases, thereby affecting the ionic conductivity. Different anions have distinct ionic radii and electron cloud distributions, which lead to changes in lattice parameters upon substitution. Even with the same central cation, halide solid electrolytes can exhibit different crystalline structures with different anions. For example, Li_3YCl_6 is a trigonal phase, whereas Li_3YBr_6 is a monoclinic phase.³⁴ Moreover, larger anion radii and higher anion polarizability can expand the lattice spacing to create a ‘softer’ lattice environment that lowers the Li^+/Na^+ migration barrier, although at the expense of reduced oxidative stability.

Mixing different halide anions can also have a significant impact on both the crystal structure and ionic conductivity. Yamada and colleagues were the first to study the effect of anion substitution on the conductivity of $Li_3InBr_{6-x}Cl_x$.⁹³ Replacing Br with Cl reduces the lattice volume and lowers the phase transition temperature. Although the reduced lattice volume typically diminishes ionic conductivity, this substitution in $Li_3InBr_{6-x}Cl_x$ enhances the ionic conductivity, primarily due to the ordered replacement of Cl, which altered the crystal symmetry or local environment to form a structure more favorable for ion transport. Similarly, Chen’s group also improved the ionic conductivity of $Li_3Y(Br_3Cl_3)$ to $7.2 \times 10^{-3} \text{ S cm}^{-1}$ through Cl and Br anion mixing combined with hot pressing.⁹⁴ This improvement is attributed to Li existing in both octahedral and tetrahedral sites, where the tetrahedral Li sites facilitate the formation of vacancies in the octahedral sites, thereby lowering the activation energy for Li^+ migration. Meanwhile, the hot pressing also optimizes the grain boundaries, so that both effects contribute together to enhance the Li^+ conduction. In addition, there are many other studies that have reported high ionic conductivities in dual-halide anion-mixed electrolytes, such as $Li_3YCl_{4.5}Br_{1.5}$ ($6.1 \times 10^{-3} \text{ S cm}^{-1}$),⁹⁵ $Li_3GdCl_3Br_3$ ($11 \times 10^{-3} \text{ S cm}^{-1}$),⁹⁵ and $Li_3HoBr_3I_3$ ($2.7 \times 10^{-3} \text{ S cm}^{-1}$).⁹⁶

For Na-based halide electrolytes, computational predictions suggest that mixing Br and I anions to induce local structural disorder could increase the ionic conductivity of $Na_3GdBr_3I_3$ to $7.5 \times 10^{-3} \text{ S cm}^{-1}$, although this compound has not yet been experimentally synthesized.⁹⁷ Furthermore, introducing F^- into the lattice produces an effect opposite to that of Cl, Br, and I. They slightly reduce the ionic conductivity but broaden the oxidation stability window. This behavior is related to the intrinsic properties of the anions, such as ionic radius and electronegativity. For example, the dual-halogen SE with fluorinated compounds such as $Li_2ZrCl_xF_{6-x}$ ^{98,99} and $Li_3InCl_{4.8}F_{1.2}$ ¹⁰⁰ can exhibit superior oxidative stability up to even 6 V (vs. Li^+/Li), which is beneficial for compatibility with a high-voltage cathode and enhanced energy density.



Due to the differences in valences, ionic radii, and electronegativities between oxide and chloride ions, oxygen doping can induce lattice distortions that alter the size and connectivity of ion diffusion channels and in some cases even cause the structure to become amorphous. For example, Jung *et al.* synthesized a high-ionic-conductivity nanocomposite solid electrolyte (HNSE), $\text{ZrO}_2\text{-(ACl)-A}_2\text{ZrCl}_6$ ($\text{A} = \text{Li or Na}$), *via* a two-step ball milling

process (Fig. 5a).¹⁰¹ Although the HNSE structure contains the ion-insulating ZrO_2 phase, the nanometer-scale ZrO_2 particles are dispersed within the Li_2ZrCl_6 matrix, creating numerous interfaces that serve as fast ion transport pathways. The conduction behavior at the $\text{ZrO}_2/\text{Li}_2\text{ZrCl}_6$ interfaces is attributed to the local substitution of oxygen ions, which widens the ion transport channels and increases the Li content at the interface.

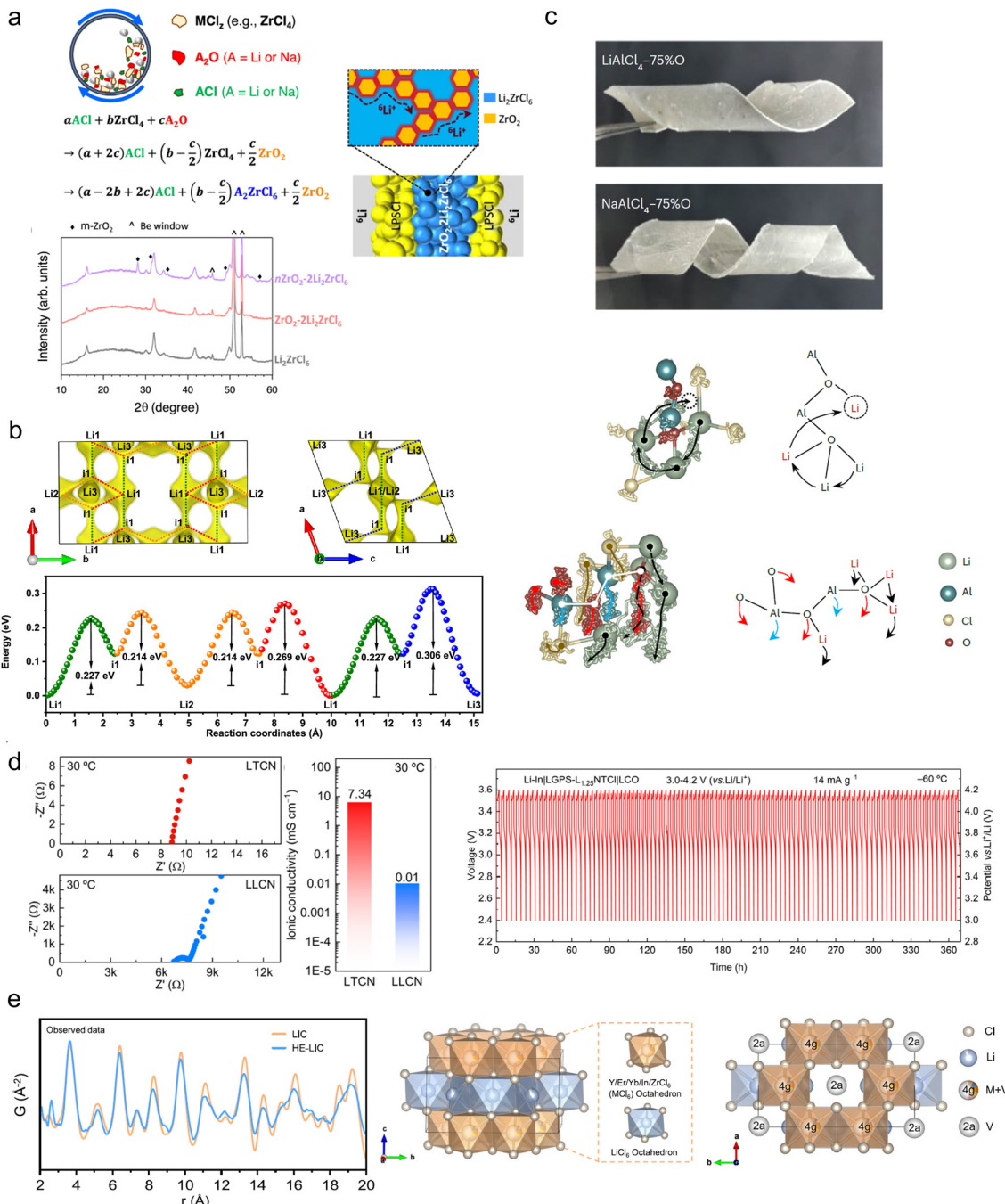


Fig. 5 (a) Preparation of $\text{ZrO}_2\text{-(ACl)-A}_2\text{ZrCl}_6$ (A = Li or Na) through a two-step ball-milling synthesis method, and the schematic diagram of the interfacial superionic Li^+ diffusion pathways.¹⁰¹ (b) Li^+ migration pathways and migration energy barriers in $\text{Li}_3\text{Zr}_{0.75}\text{OCl}_4$.¹⁰² (c) The hopping and migration of Li^+ in the viscoelastic electrolytes LACO and NACO.³⁹ (d) The high ionic conductivity and excellent extremely low temperature performance of amorphous nitrogen-halide electrolytes $\text{Li}_{3x}\text{TaCl}_5\text{N}_x$.^{105,106} (e) The local structure and unit cell of HE-LIC.¹⁰⁷



This section will mainly describe crystalline oxyhalide electrolytes, while the amorphous oxyhalide electrolytes will be discussed in detail in Section 4.3. Tanaka's group fabricated orthorhombic LiMOC_4 ($\text{M} = \text{Nb}, \text{Ta}$) *via* ball milling with subsequent sintering, achieving a superior room-temperature ionic conductivity exceeding $10 \times 10^{-3} \text{ S cm}^{-1}$ as well as a high oxidative stability window of 5 V *vs.* Li^+/Li .³⁸ Furthermore, a series of low-cost Zr-based oxychloride electrolytes have been reported, including $\text{Li}_3\text{Zr}_{0.75}\text{OCl}_4$,¹⁰² $\text{Li}_{2.22}\text{Zr}_{1.11}\text{O}_{0.67}\text{Cl}_{5.33}$ ¹⁰³ and $\text{Li}_{3.1}\text{ZrCl}_{4.9}\text{O}_{1.1}$,¹⁰⁴ all of which exhibit monoclinic structures and ionic conductivities exceeding $10^{-3} \text{ S cm}^{-1}$. $\text{Li}_3\text{Zr}_{0.75}\text{OCl}_4$ was synthesized by substituting the Sc^{3+} ions with 0.75 Zr^{4+} in Li_3ScCl_6 and compensating for the cation vacancies by replacing a small amount of Cl with O (Fig. 5b).¹⁰² The non-periodic features and the crystalline phase (monoclinic structure) synergistically promote ion conduction and facilitate Li^+ transport. Similarly, $\text{Li}_{2.22}\text{Zr}_{1.11}\text{O}_{0.67}\text{Cl}_{5.33}$ and $\text{Li}_{3.1}\text{ZrCl}_{4.9}\text{O}_{1.1}$ are both produced *via* oxygen substitution that induces a phase transformation from the trigonal to the monoclinic structure, which stabilizes the tetrahedral lithium sites and shortens the Li^+ hopping distance to enhance the conductivity.

4.3 Amorphization

Amorphization is another efficient strategy to improve the carrier transport by affording abundant intrinsic defects, few grain boundaries, and large transport spaces. There are various strategies to prepare halide-based electrolytes with amorphous structures such as extending the mechanochemical process as mentioned in the previous section or introducing divalent oxygen or trivalent nitrogen into halides, thereby enhancing the ionic conductivity.

Oxyhalides have emerged as a promising solid electrolyte system over the past three years, exhibiting unique structural and performance advantages. The element oxygen plays a critical role due to its strong ability to form amorphous structures and preferentially connect metal polyhedra over short distances in the form of bridging oxygen, which contributes to high ionic conductivity. Currently, oxyhalide electrolytes are mainly reported based on the metal cations, such as Al, Ta, Nb, Hf and Zr, as well as antiperovskite structures $\text{Li}/\text{Na}_3\text{OX}$ ($\text{X} = \text{Cl}, \text{Br}, \text{I}$).

Our group first proposed a class of viscoelastic inorganic glass electrolytes (VIGLAS) using aluminum-based compounds $\text{LiAlCl}_{4-2x}\text{O}_x$ (LACO) and $\text{NaAlCl}_{4-2x}\text{O}_x$ (NACO), whose ionic conductivities are $1.52 \times 10^{-3} \text{ S cm}^{-1}$ and $1.33 \times 10^{-3} \text{ S cm}^{-1}$, respectively.³⁹ By introducing varying amounts of oxygen element to sodium/lithium tetrachloroaluminate to replace part of Cl with O, the materials transformed from a brittle molten salt into a ductile glass at room temperature as the oxygen content increased, as shown in Fig. 5c. The high ionic conductivity is attributed to the introduced O, which shortens the distance between Li–Li, allowing Li^+ to hop over a shorter distance. On the other hand, the vibration of the Al–O–Al chains facilitates the simultaneous migration of surrounding Li^+ and Cl^- , thus promoting ion transport. Moreover, all the

elements involved in the VIGLAS are Earth-abundant elements, so that the materials have the lowest cost compared to other reported inorganic SEs. This finding is a milestone that simultaneously achieved the merits of inorganic and polymer electrolytes, which has gained wide recognition from researchers.^{108–110} Subsequently, Sun's group synthesized a series of amorphous $\text{LiAlO}_x\text{Cl}_y$ electrolytes with ionic conductivities exceeding $10^{-3} \text{ S cm}^{-1}$ using different methods, such as the self-propagating method (simply pressing followed by sintering), the crystal water-assisted method (using $\text{LiCl}-\text{AlCl}_3-\text{AlCl}_3\cdot 6\text{H}_2\text{O}$), and low-temperature sintering of Li_2O_2 with AlCl_3 .^{111–113} Nazar and colleagues also prepared an aluminum-based oxychloride electrolyte ($\text{LiAlCl}_4-\text{AlCl}_3-\text{AlCl}_3\cdot 6\text{H}_2\text{O}$) with plasticity *via* solid-state sintering.¹¹⁴ This method can also be extended to Na^+ conductors and Na–K mixed ion conductors.

Furthermore, there are various other reported amorphous oxyhalide electrolytes $\text{Li}/\text{NaMO}_x\text{Cl}_y$ ($\text{M} = \text{Ta}, \text{Nb}, \text{Hf}, \text{Zr}$) with high ionic conductivities ranging from 10^{-4} to $10^{-3} \text{ S cm}^{-1}$ by supplying an oxygen source through different oxygen-containing lithium or sodium salts (*e.g.*, Li_2O , $\text{Li}_2\text{O}_2/\text{Na}_2\text{O}_2$, LiOH/NaOH) *via* ball milling or sintering, as shown in Table 2. In addition, $\text{Li}_{2.5}\text{ZrCl}_5\text{F}_{0.5}\text{O}_{0.5}$ synthesized by dual doping with fluoride and oxide anions into Li_2ZrCl_6 exhibits a high ionic conductivity of $1.17 \times 10^{-3} \text{ S cm}^{-1}$ and excellent voltage stability (up to 4.87 V *vs.* Li^+/Li).¹¹⁵ In this case, the incorporation of F improves high-voltage stability, while the introduction of O induces the structure toward amorphization and reduces crystallinity to 24.6%. This disordered structure mitigates the negative impact of F on conductivity.

Beyond the oxygen substitution, nitrogen doping can also induce the formation of an amorphous phase. Han *et al.* reported a class of amorphous nitrogen-halide electrolytes $\text{Li}_{3x}\text{TaCl}_5\text{N}_x$ with high ionic conductivities up to $7.34 \times 10^{-3} \text{ S cm}^{-1}$ (Fig. 5d).¹⁰⁶ This improvement is mainly due to the introduction of nitrogen altering the coordination environment between cations and anions, thereby facilitating the Li^+ transport. This electrolyte also exhibits excellent performance

Table 2 Amorphous oxyhalide electrolytes with different oxygen sources

Oxyhalide electrolytes	Oxygen source	Conductivity (mS cm^{-1})	Ref.
$\text{LiAlCl}_{2.5}\text{O}_{0.75}$	Sb_2O_3	1.52	39
$\text{NaAlCl}_{2.5}\text{O}_{0.75}$	Sb_2O_3	1.33	39
$\text{AlOCl}-\text{nanoLiCl}$	Li_2O_2	1.02	113
$\text{LiAlOCl}-981$	$\text{AlCl}_3\cdot 6\text{H}_2\text{O}$	1.04	112
$\text{AOC}-2\text{LiCl}$	Sb_2O_3	1.24	111
$\text{PLAOCl}^{0.3b}$	$\text{AlCl}_3\cdot 6\text{H}_2\text{O}$	1.3	114
$1.6\text{Li}_2\text{O}-\text{TaCl}_5$	Li_2O	6.6	37
$1.6\text{Li}_2\text{O}-\text{HfCl}_4$	Li_2O	1.97	37
NaTaOCl_4	NaOH	1.2	44
$\text{Na}_2\text{O}_2-\text{HfCl}_4$	Na_2O_2	0.52	80
$\text{Na}_2\text{O}_2-\text{ZrCl}_4$	Na_2O_2	0.42	80
$\text{Na}_2\text{O}_2-\text{TaCl}_5$	Na_2O_2	2	80
$0.5\text{Na}_2\text{O}_2-\text{TaCl}_5$	Na_2O_2	4.62	116
$\text{Li}_{2.5}\text{ZrCl}_5\text{F}_{0.5}\text{O}_{0.5}$	Li_2O	1.17	115



under extremely low temperatures, maintaining stable charge/discharge cycles for over 200 hours at -60°C .¹⁰⁵

4.4 Designing high-entropy configurations

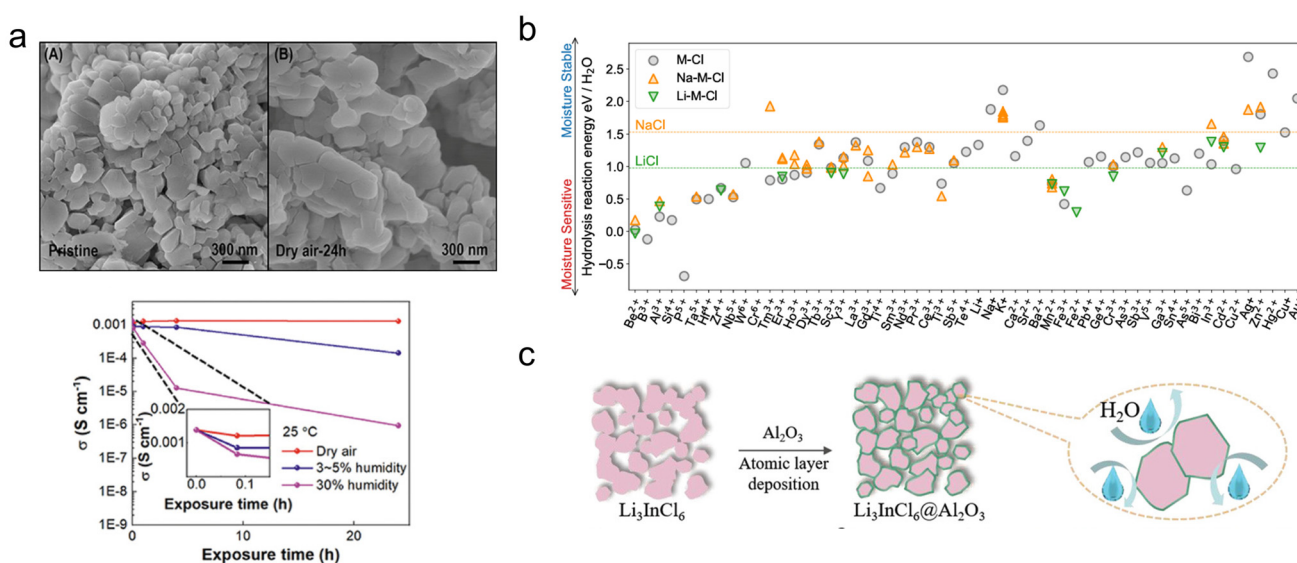
High-entropy materials typically consist of five or more metal elements and have a configuration entropy $\Delta S \geq 1.5R$ (R is the ideal gas constant). The high-entropy strategy can promote disorder in the arrangement of Li^+ and vacancies, locally disrupting the site energy by introducing disorder and distortion, which make the energy levels of adjacent sites overlap and therefore reduce the activation energy. Typically, metal cations with similar ionic radii but varied valence states are selected to facilitate the formation of solid solutions. Currently, research on high-entropy halide electrolytes is still in early stages, and only a few materials have been reported. For example, Luo and colleagues synthesized a high-entropy electrolyte, $\text{Li}_{2.75}\text{Y}_{0.16}\text{Er}_{0.16}\text{Yb}_{0.16}\text{In}_{0.25}\text{Zr}_{0.25}\text{Cl}_6$, which exhibits an ionic conductivity of $1.71 \times 10^{-3} \text{ S cm}^{-1}$.¹⁰⁷ The introduction of multiple cations with different radii leads to lattice distortions that increase the migration pathways for Li^+ . In addition, the incorporation of high-valence Zr introduces more lithium vacancies, and the increased Li-Cl bond length makes them more prone to breaking, thereby forming active sites for Li^+ migration (Fig. 5e). Moreover, the restricted vibrational range of Cl^- reduces spatial hindrance. These combined factors make this high-entropy material exhibit a high ionic conductivity. Similarly, Yang's group employed a high-entropy strategy to simultaneously enhance the high-voltage stability (up to 4.8 V vs. Li^+/Li) and ionic conductivity of halide electrolytes.¹¹⁷ They synthesized a $\text{Li}_{2.9}\text{In}_{0.75}\text{Zr}_{0.1}\text{Sc}_{0.05}\text{Er}_{0.05}\text{Y}_{0.05}\text{Cl}_6$ electrolyte with an ionic conductivity of up to $2.18 \times 10^{-3} \text{ S cm}^{-1}$ and proposed that increasing configuration entropy and reducing oxidative by-products can effectively enhance the oxidation stability.

5. Chemical and electrochemical stability of halide-based electrolytes

5.1 Air/humidity stability

In recent years, halide-based electrolytes have primarily focused on enhancing ionic conductivity and electrochemical stability, as well as exploring the optimization of ion transport mechanisms. However, due to the high hygroscopicity and deliquescence of halide-based electrolytes and their raw materials, their synthesis must strictly rely on an inert atmosphere. In addition, the degradation products of halide-based electrolytes are highly corrosive, which significantly increases the industrial costs and technical complexity. Furthermore, the moisture-induced degradation process involves a complex, multiscale gas-solid interfacial reaction network, and a systematic understanding of the interaction mechanisms between halide-based electrolytes and air is still lacking.

Li_3InCl_6 is recognized as one of the most air-stable electrolytes and can even be directly synthesized *via* an aqueous solution method. However, as shown in Fig. 6a, in dry air, Li_3InCl_6 shows no significant changes in particle morphology and ionic conductivity within 24 h.¹¹⁸ As ambient humidity increases, its ionic conductivity declines markedly. Particularly, when the humidity reaches 30%, the ionic conductivity rapidly drops to $10^{-6} \text{ S cm}^{-1}$ and the activation energy increases, indicating that Li^+ transport becomes more difficult. This is because Li_3InCl_6 reacts with the moisture in the air to form In_2O_3 , LiCl , and HCl . It can also absorb water to form the hydrate $\text{Li}_3\text{InCl}_6 \cdot x\text{H}_2\text{O}$, which reduces its ionic conductivity. Consequently, Li_3InCl_6 exhibits better air stability in low-humidity environments or dry rooms, and the hydrate $\text{Li}_3\text{InCl}_6 \cdot x\text{H}_2\text{O}$ formed upon water absorption is reversible with



Li_3InCl_6 . Once the crystallization water is removed *via* vacuum drying, the ionic conductivity can be fully restored.³⁵ So far, this is the only halide-based electrolyte that can directly form a hydrate intermediate and undergo reversible chemical transformation. Other halide-based electrolytes decompose directly into $\text{MCl}_y \cdot x\text{H}_2\text{O}$ and $\text{LiCl} \cdot x\text{H}_2\text{O}$, where $\text{MCl}_y \cdot x\text{H}_2\text{O}$ further decomposes into M_2O_3 and HCl during dehydration.^{120,121} Similarly, in $\text{Li}_3\text{Y}_{1-x}\text{In}_x\text{Cl}_6$, where In^{3+} partially substitutes for Y^{3+} , increasing the substitution level transforms the electrolyte's structure from the hcp to the ccp anion sublattice, thereby improving the moisture resistance.⁵⁹ This is primarily because the ccp-type $\text{Li}_3\text{Y}_{1-x}\text{In}_x\text{Cl}_6$ first forms a hydrate intermediate $\text{Li}_3\text{Y}_{1-x}\text{In}_x\text{Cl}_6 \cdot \text{H}_2\text{O}$ after absorbing water, which can be reversibly converted back to $\text{Li}_3\text{Y}_{1-x}\text{In}_x\text{Cl}_6$ upon high-temperature dehydration. Additionally, computational analysis of hydrolysis reaction energies have shown that in lithium-based ternary chlorides, cations such as In^{3+} , Ga^{3+} , Zn^{2+} , and Cd^{2+} exhibit excellent moisture resistance, while in sodium-based ternary chlorides, lanthanide cations like Tm^{3+} and Tb^{3+} provide good moisture resistance (Fig. 6b).¹¹⁹ Ma *et al.* found that Li_2ZrCl_6 also has good moisture resistance even after being exposed to a nitrogen environment with 5% humidity for 24 h.³⁶ Its structure remained unchanged and the ionic conductivity could still remain at $0.81 \times 10^{-3} \text{ S cm}^{-1}$. However, in contrast to Li_2ZrCl_6 , Li_3InCl_6 quickly formed hydrates under the same conditions, resulting in a one-order-of-magnitude drop in ionic conductivity. Beyond synthesizing halide-based electrolytes that are intrinsically resistant to air and moisture, the issue can also be mitigated by adjusting the contact area and composition of the solid–gas interface. For example, depositing a layer of Al_2O_3 on Li_3InCl_6 effectively isolates the electrolyte from direct contact with air, greatly enhancing its air stability (Fig. 6c).¹²⁰ Currently, strategies to improve the air/moisture stability of halide-based electrolytes are relatively limited, and more explorations are expected in the future.

5.2 Intrinsic electrochemical stability

The electrochemical stability window (ESW) of halide-based electrolytes is a key parameter affecting the electrochemical performance of ASSBs. Depending on the halide anions, the order of ESW width is generally determined as $\text{F} > \text{Cl} > \text{Br} > \text{I}$. Both theoretical calculations and experimental data have demonstrated that fluoride- and chloride-based electrolytes exhibit high oxidation stability, exceeding 6 V *vs.* Li^+/Li and 4 V *vs.* Li^+/Li , respectively (Fig. 7a).⁷⁵ For the $\text{Na}-\text{M}-\text{X}$ ($\text{X} = \text{F}, \text{Cl}, \text{Br}, \text{I}, \text{O}, \text{S}$), thermodynamic calculations of the intrinsic ESW for the various anions in the structure indicate that nearly all such electrolytes exhibit oxidation stability over 3 V *vs.* Na^+/Na , except for iodide-based electrolytes (Fig. 7b).¹²² For example, the electrochemical windows of Na_3YCl_6 and Na_3YBr_6 are 0.51–3.75 V *vs.* Na^+/Na and 0.57–3.36 V *vs.* Na^+/Na , respectively.¹²² However, halide-based electrolytes also suffer from a critical drawback of relatively poor electrochemical reduction stability. Their high reduction potentials make them unsuitable for direct contact with metallic lithium or sodium anodes. The extent to which the reduction potential is limited mainly depends on the reduction potential

of the central metal cations. Thermodynamic calculations have shown that group IIIB cations (such as Sc^{3+} and Y^{3+}) exhibit relatively good reduction stability.¹²³ It is worth noting that in practical applications, the formation of effective interfacial passivation layers and favorable interfacial kinetics can also result in an actual ESW that surpasses the theoretical stability limits, which should be considered integrally.

5.3 Interfacial stability

In addition to the important influence of the intrinsic properties of halide-based electrolytes, the poor interfacial contact with electrode materials and the issues with interfacial chemical stability are also the key factors limiting their development. Unlike the good wettability of liquid electrolytes, the contacts between SEs and electrode materials are point contacts, resulting in small contact areas that lead to high interfacial resistance and directly reduce the migration pathways for Li^+/Na^+ while causing stress accumulation. Moreover, when the electrode potential exceeds the electrolyte's intrinsic electrochemical stability window, spontaneous interfacial reactions will occur. There are three different types of interfaces that can be formed between electrodes and electrolytes (Fig. 7c). The first is that the electrolyte and electrode are thermodynamically stable, indicating that no reaction occurs to form interfacial components. The second is that although the electrode and electrolyte are not thermodynamically stable, the generated interfacial components are ionically conductive and electronically insulating. The third type is the interfacial components within mixed electronic and ionic conductors, which lead to continuous reactions until the electrolyte is completely consumed, and obviously, should be strictly avoided. In practice, the first type of interface is difficult to achieve especially at the anode side since metallic lithium or sodium anodes have the lowest chemical potentials. The second type of interface is the most possible one, where a passivation layer can form to extend the ESW of the electrolyte.

Due to the high oxidative stability of halide-based electrolytes, they can typically come into direct contact with oxide cathodes without additional surface coatings. Asano *et al.* first matched Li_3YCl_6 with uncoated LiCoO_2 achieving an initial coulombic efficiency as high as 94.8% and a low interfacial resistance of $16 \Omega \text{ cm}^{-2}$ (Fig. 7d).³⁴ In addition, cathodes such as $\text{LiNi}_{0.6}\text{Mn}_{0.2}\text{Co}_{0.2}\text{O}_2$, $\text{LiNi}_{0.8}\text{Mn}_{0.1}\text{Co}_{0.1}\text{O}_2$, $\text{LiNi}_{0.83}\text{Mn}_{0.05}\text{Co}_{0.12}\text{O}_2$ and $\text{LiNi}_{0.88}\text{Al}_{0.01}\text{Co}_{0.11}\text{O}_2$ have also been reported to be compatible with halide-based electrolytes.^{69,92,126–128} However, cathode active materials with different structures and varying transition metal contents exhibit significant differences in interfacial stability with halide-based electrolytes (Fig. 7e).^{123,125} For example, a tantalum-based oxychloride electrolyte (LTOC) paired with Ni-rich NCM83 cathodes shows the optimal compatibility although the LTOC/NCM83 interface is thermodynamically unstable (Fig. 8a).¹²⁹ This is due to the formation of a functional interfacial passivation layer (*e.g.* $\text{Li}-\text{Ta}-\text{O}$ compounds) which suppresses further decomposition. In contrast, when LTOC is matched with a LiCoO_2 cathode, inter-diffusion of Co and Ta occurs at the interface, and the generated byproducts, such as

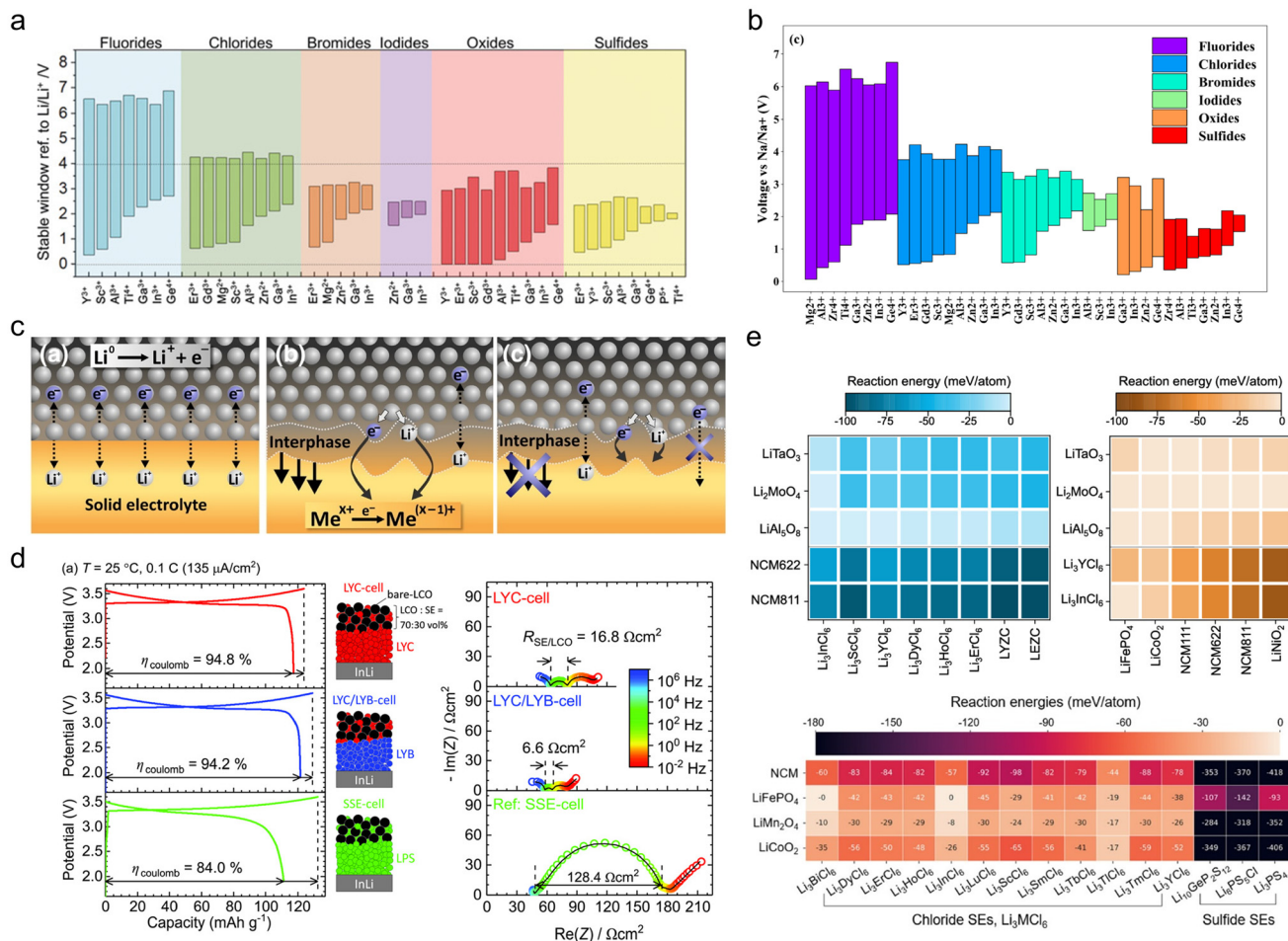


Fig. 7 The thermodynamic electrochemical windows of (a) Li-M-X (X = F, Cl, Br, I, O, S)⁷⁵ and (b) Na-M-X through calculation.¹²² (c) Three types of interfaces between lithium metal and solid electrolytes.¹²⁴ (d) Initial charge/discharge curves and the impedance value of Li₃YCl₆ after the first charging cycling.³⁴ (e) The reaction energy calculations between different cathode materials and halide electrolytes based on various metal cations.^{123,125}

Ta₂CoO₆, lead to instability of the interface. Lowering the operating temperature can reduce the reactivity of these interfacial reactions. Moreover, the physical contact between the halide-based electrolyte and the cathode particles significantly affects the electrochemical performance. A well-designed composite cathode with an appropriate composition ratio and uniform mixing of the active cathode material and catholyte is one of the key factors in constructing a continuous interlinked network for both ion and electron diffusion. The contact morphology and microstructure among the composite cathode particles can greatly influence the electrochemical performance of ASSBs. During electrochemical cycling, the cathode active material typically undergoes volume changes due to variations in Li/Na content, which generates internal stress and results in a loss of contact between the electrolyte and the cathode active particles, thereby degrading cycling stability. Compared with polycrystalline cathode active materials, monocrystal cathodes offer better high-voltage tolerance and higher mechanical stability, which can help prevent contact loss in composite cathodes. In contrast,

polycrystalline cathode particles are prone to particle breakage during the preparation and compaction processes, and they also exhibit anisotropic volume strain during cycling, leading to intergranular cracks that will reduce the ion transport kinetics and increase the interfacial impedance. For example, Jung's group investigated the performance differences between monocrystal and polycrystalline Ni-rich oxide cathodes (NCA) paired with Li₃YCl₆ in ASSBs (Fig. 8b).¹²⁷ They found that the combination of monocrystal NCA with Li₃YCl₆ achieved stable long-term cycling with a capacity retention of 96.8% after 200 cycles. This outstanding performance is mainly attributed to the dense, grain-boundary-free structure of the monocrystal materials, which significantly enhances their resistance to volume strain, while the morphology of the monocrystal particles prevents local stress concentration caused by particle agglomeration. Tables 3 and 4 respectively summarize the typical cathode compositions and electrochemical performances of current Li- and Na-based halide electrolytes, offering an intuitive view of their development at this stage.



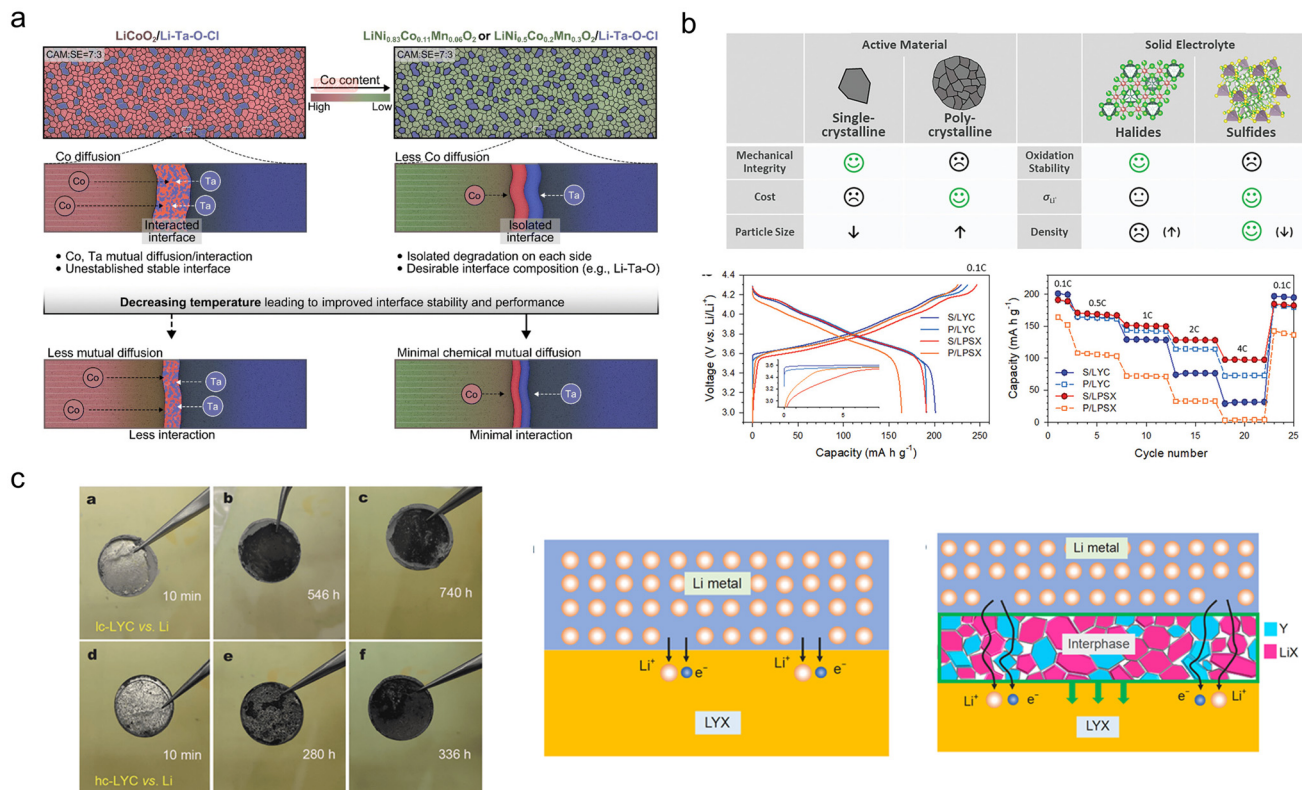


Fig. 8 (a) Schematic diagram of the interface between LTOC and cathode materials with different Co contents at different temperatures.¹²⁹ (b) Effect of monocrystal and polycrystalline cathodes on compatibility with halide-based electrolytes.¹²⁷ (c) Interfacial reaction phenomena between Li_3YX_6 and the metallic lithium anode.¹³⁰

As mentioned above, most halide-based electrolytes exhibit poor reduction stability and are thermodynamically unstable with metallic lithium/sodium and alloy anodes (e.g., Li_xIn , Na_xSn). Therefore, understanding the reaction mechanisms between these electrolytes and the anodes is of utmost importance. For example, Ma *et al.* investigated the reaction mechanism between Li_3YX_6 ($\text{X} = \text{Cl}, \text{Br}$) and metallic lithium anodes and found that the thermodynamic incompatibility arises because Li_3YX_6 is reduced to form metal Y and LiX , creating an interfacial phase that is a mixed ionic and electronic conductor, which leads to a continuous interfacial reaction during the cycling (Fig. 8c).¹³⁰ Similarly, Li_3InCl_6 reacts with metallic lithium to form LiCl and In. In the $\text{Li}|\text{Li}_3\text{InCl}_6|\text{Li}$ symmetric cell, the interfacial resistance was observed to continuously increase over time and reach a total resistance as high as 854 Ω after just one hour.¹³¹

The stability of halide-based electrolytes against anodes can be improved by constructing an interfacial buffer layer. Currently, the most commonly used method is to combine halide-based electrolytes with sulfide-based electrolytes ($\text{Li}_6\text{PS}_5\text{Cl}$, $\text{Li}_{10}\text{GeP}_2\text{S}_{12}$, Na_3PS_4 , etc.) to form a dual-electrolyte layer, although it should be noted that interfacial instability also exists between halide-based and sulfide-based electrolytes.^{106,112,116} Besides sulfide-based electrolytes, nitride-based electrolytes have also been demonstrated to be

effective as modification layers. The vacancy-rich $\beta\text{-Li}_3\text{N}$ ¹³² and $\text{Li}_9\text{N}_2\text{Cl}_3$ ¹³³ and the oxyhalide nitride solid electrolyte $\text{Li}_3\text{N}_y\text{I}_z\text{-qLiOH}$ ¹³⁴ reported both show high stability to metallic lithium anodes, which achieved long-term stable lithium plating/stripping. Moreover, owing to their softer sublattice and lower reduction potential, iodide-based electrolytes such as cubic Li_4YI_7 also show good compatibility with lithium metal.¹³⁵ At present, only a few halide-based electrolytes have achieved stability on the anode side, but they could not achieve stability on both cathode and anode materials at the same time. They still need to be used in combination with other oxidation-resistant halide-based electrolytes.

6. Advanced characterization techniques

Developing high-performance halide-based electrolytes requires an in-depth understanding of their structures, ion diffusion pathways, and transport mechanisms. Moreover, to realize commercially viable halide-based solid-state batteries, it is also crucial to investigate the evolution and degradation of the internal structures and interfaces of halide-based electrolytes during cycling. Electrochemical characterization forms the foundation for understanding solid-state battery materials.




Table 3 Li-based halide electrolyte all-solid-state battery cell assembly parameters and electrochemical performances

Halide-based electrolytes	Cathodes	Carbon additive	Weight ratio of composite cathodes	Cathode loading	Cycling pressure/ MPa	Cycling temperature/°C	Cycling performance	Ref.
LiAlCl _{2.5} O _{0.75}	NCM622	CNT	20:70:5:5 (PTFE)	4 mg cm ⁻² —	60	Charged to 4.3 V at 1 °C and cycled 600 times	39	
Li _{2.1} Zr _{0.95} Cl _{0.05} O _{0.8}	SC-NCM83	—	30:70	7–9 mg	25	Retained 90.3% capacity after 1000 cycles within a voltage range of 2.8–4.3 V at 2 °C	139	
Li _{0.388} Ta _{0.238} La _{0.475} Cl ₃	SC-NCM523	VGCF	30:65:2:3 (PTFE)	7.06 mg cm ⁻²	—	Li/Li _{0.388} Ta _{0.238} La _{0.475} Cl ₃ /NCM523 can be cycled for more than 100 cycles with 81.6% capacity retention	71	
LiAlOCl-981	SC-NCM88	Carbon black	30:70:1	10 mg	200	Charged to 4.3 V at 0.5 °C and sustained 84.86% capacity after 1500 cycles	112	
Li _{1.25} TaCl ₅ N _{0.417}	LCO	VGCF	25:70:5	5 mg	0.5 ton	Achieved a capacity retention of 83.13% after 1200 cycles at 1 °C and –20 °C	106	
Li _{1.75} Zr _{0.75} Ta _{0.25} Cl ₆	NMC88	—	3:7	8.92 mg cm ⁻²	1.5 ton	Retained 90.6% of the initial capacity after 1600 cycles at 2 °C	140	
Li _{2.75} Y _{0.16} Er _{0.16} Yb _{0.16} In _{0.25} Zr _{0.25} Cl ₆	LCO	—	3:7	8 mg	—	Charged to 4.6 V and delivered an initial capacity of 185 mAh g ⁻¹ and maintained a capacity retention of 91.6% over 50 cycles	107	

In addition, a variety of advanced *in situ* and *ex situ* characterization techniques can be employed to study the structural, morphological, and other properties of solid-state electrolytes and their interfaces with electrodes. Beyond experimental techniques, computational methods such as density functional theory (DFT), *ab initio* molecular dynamics (AIMD) and bond valence sum evaluation (BVSE) can be used to simulate structures and Li⁺/Na⁺ transport pathways within electrolytes, providing further support for experimental findings. The following section outlines several advanced characterization techniques used to describe structural information in halide-based electrolytes.

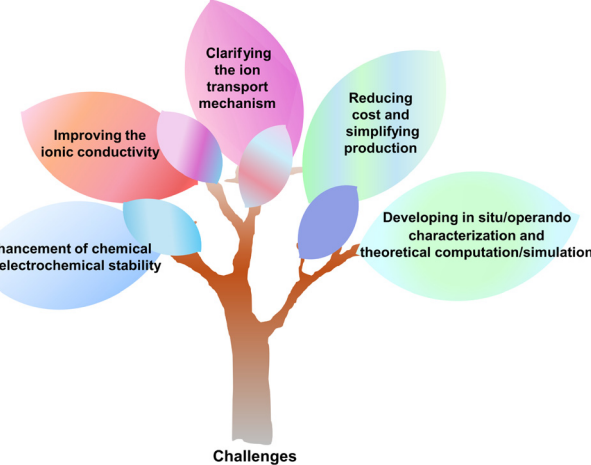
X-ray diffraction (XRD) performs exceptionally well in detecting heavy atoms such as metals or halogens, but it is relatively insensitive to light elements. In contrast, neutron powder diffraction (NPD) plays an indispensable role in identifying the distribution and occupancy of light elements like Li⁺/Na⁺ in newly crystal structures, as well as in elucidating their migration pathways, due to its high sensitivity to light atoms.¹³⁶ For example, Yao *et al.*⁷¹ used synchrotron X-ray diffraction to identify Ta, La, Cl, and particularly La/Ta vacancies to confirm the overall lattice framework in Li_{0.388}Ta_{0.238}La_{0.475}Cl₃. Meanwhile, neutron data were employed to determine the lithium distribution, revealing two distinct Li sites in the structure. Furthermore, based on the NPD determined structure, bond valence site energy (BVSE) analysis showed that lithium migrates not only along 1D channels but also between adjacent channels *via* La vacancies.

Pair distribution function (PDF) analysis is a powerful technique for resolving atomic-scale structures of halide-based electrolytes, particularly those that are amorphous or locally disordered. It reveals both short-range and medium-range order in materials, overcoming the limitation of the conventional XRD which only probes long-range order. PDF provides valuable information on average atomic pair distances within locally ordered units in amorphous phases. For instance, Sun *et al.*⁴¹ used PDF analysis to show that on increasing the ball-milling time of NaTaCl₆, besides an increase in the ionic conductivity, the medium-range peak features (5–20 Å) gradually weakened, indicating that the structure is more disordered. Meanwhile, an enhancement of the Cl–Cl scattering (peaks at 3.5–4 Å) suggested a denser packing of TaCl₆ octahedra and the gradual formation of a poly-(TaCl₆) octahedral network, which constitutes a sodium-conducting amorphous framework.

In addition, solid-state nuclear magnetic resonance (NMR) and X-ray absorption spectroscopy (XAS) are essential for probing local coordination and bonding environments. XAS can analyze bond length variations *via* Fourier-transformed R-space data, while solid-state NMR distinguishes local coordination environments through chemical shifts. Furthermore, 2D NMR spectroscopy can trace Li⁺ migration pathways at the atomic level. For example, using 2D ⁷Li EXSY exchange NMR, Sun's group discovered that the introduction of lithium carbonate promotes lithium exchange both between amorphous domains and between amorphous and crystalline phases in

**Table 4** Na-based halide electrolyte all-solid-state battery cell assembly parameters and electrochemical performances

Halide-based electrolytes	Cathodes	Carbon additive	Weight ratio of composite cathodes	Cathode loading	Cycling pressure/MPa	Cycling temperature/°C	Cycling performance	Ref.
NaAlCl _{2.5} O _{0.75}	NVOPF	CNT	20:70:10:5(PTFE)	3.3 mg cm ⁻²	—	60	Charged to 4.3 V at 1 C and cycled 600 times with a retention of 83.5%	39
0.5Na ₂ O ₂ -TaCl ₅	NMNF0	CNT	40:60, 2 wt%CNT	8 mg	80	25	Charged to 3.8 V and retained 66% capacity after 500 cycles at 0.1 C	116
Na ₂ O ₂ -HfCl ₄	NMNF0	CNT	40:60, 2 wt%CNT	8 mg	110	—	Maintained 78% capacity retention over 700 cycles at 0.2 C	80
2NaF-ZrCl ₄	NFM	Super P	30:70, 5 mg Super P	5.7 mg cm ⁻²	—	25	Charged to 4.3 V at 0.2 C and sustained 81.1% capacity after 600 cycles	141
Na _{0.25} Y _{0.25} Zr _{0.75} Cl ₄	NaCrO ₂	VGCF	16:11:0.5	—	50-70	23	Achieved a capacity retention of 83% after 500 cycles at 1 C	49
Na _{0.7} Zr _{0.3} La _{0.7} Cl ₄	NaCrO ₂	Super P	50:50:3	12 mg	—	30	Retained 88% of the initial capacity after 70 cycles at 0.3 C	77
0.62[Na _{0.75} Sm _{1.75} Cl ₆]-0.38[NaTaCl ₆]	NMNF0	Carbon black	40:60:2	7 mg	80	25	Showed capacity retention of 88.3% after 100 cycles at 0.2 C	78

**Fig. 9** The schematic diagram of the challenges faced by halide-based electrolytes.

the oxyhalide-based AlOCl-2LiCl (LAOC) electrolyte.¹³⁷ This resulted in an accelerated movement of ions at various lithium sites, indicating an enhanced ion transport and an improved interface dynamics.

7. Conclusions and outlook

This review summarized the latest progress in Li-based and Na-based halide electrolytes. Firstly, it outlined the commonly used synthesis methods, which mainly include solid-state synthesis (mechanical milling, sintering and their combination) and liquid-phase synthesis (water-mediated and ammonium-assisted wet chemistry), with solid-state synthesis being predominant. Mechanical milling can induce local structural distortions and disorder to enhance ionic conductivity while also ensuring a more uniform mixing of precursors, thereby reducing the sintering time. In contrast, among liquid-phase synthesis methods, only Li₃InCl₆ can be synthesized using a water-mediated approach, which cannot be generalized to other systems. Secondly, we classified the existing halide-based electrolytes into three categories based on structural differences, and we described in detail the ion transport mechanisms through representative electrolyte materials. The structures are mainly composed of close-packed anion frameworks (ccp, hcp), non-close-packed anion frameworks of the UCl₃-type, and amorphous structures. The transport mechanism is primarily based on a vacancy-mediated process. In addition, we provided a detailed overview of strategies for enhancing ionic conductivities and optimizing ion transport. Ionic conductivity can be effectively improved by doping with isovalent or aliovalent cations/anions, introducing vacancy defects or increasing carrier concentrations, or converting the structures into amorphous phases. Finally, we discussed the challenges and failure mechanisms faced by the air stability of halide-based electrolytes and the interfacial stability with both

cathode and anode materials. The thermodynamic stability of halide-based electrolytes mainly depends on the oxidation potential, which is influenced by the anions, and the reduction potential that is affected by the central metal cations. In practical applications, interfacial stability is not only determined by the intrinsic electrochemical window but also by the stability of the interfacial products. While most halide-based electrolytes exhibit high oxidative stability, only a few are compatible with metallic lithium/sodium.

Despite the impressive progress in ionic conductivity and oxidative stability, halide-based electrolytes still face many practical challenges (Fig. 9). First, the raw materials used for synthesizing halide-based electrolytes often involve expensive rare-earth elements, resulting in high cost. Although more abundant and cheaper halide electrolytes based on elements such as Zr and Al have emerged with merits in recent years, which can achieve high ionic conductivity and low cost, these electrolytes are extremely sensitive to ambient humidity. They are prone to irreversible hydrolysis, which leads to structural degradation, a rapid decline in ionic conductivity, and corrosion of current collectors and casings, posing significant challenges for large-scale production. Moreover, the synthesis of halide-based electrolytes currently mainly relies on mechanical milling and solid-state sintering, with only Li_3InCl_6 being amenable to water-mediated liquid-phase synthesis. The complexity of the synthesis process further limits their scalability. Regarding the intrinsic properties of halide-based electrolytes, most Li-based halide electrolytes exhibit ionic conductivity around $10^{-3} \text{ S cm}^{-1}$, and there are also several materials that can deliver a very high ionic conductivity of over $10^{-2} \text{ S cm}^{-1}$, which is comparable to those of liquid electrolytes. However, Na-based halide electrolytes generally have lower ionic conductivities and fewer available compositions. Due to the limitations in advanced characterization techniques, the ion transport mechanisms remain unclear, and the systematic understanding of the quantitative relationship between lattice dynamics and defect effects is lacking. These still largely rely on computational simulations.

Furthermore, the solid-solid interface between halide-based electrolytes and the electrodes is still the most important problem, and the operation of the batteries requires a high external pressure. These require the deep understanding and rational design of viscoelastic electrolytes with high ionic conductivities to form the conformal interfaces and improve the solid-solid contact and interfacial ion transport. Besides, increasing the poor reduction stability of halide-based electrolytes is also an urgent task. This involves the consideration of both thermodynamic and dynamic aspects. In particular for all-solid-state Na batteries (ASSNBs), metallic sodium not only has poor cycling stability but also has a low melting point below 100 °C and is unstable even in dry air, which significantly limit the cycle life and enhance the safety hazard of ASSNBs in large-scale energy storage.¹³⁸ Therefore, more stable and safer anodes such as hard carbon should be considered for the energy storage applications in ASSBs, whose interface with the halide-based electrolytes needs to be further studied.

Overall, current research indicates that halide-based electrolytes are still at their early stage, and many critical challenges must be overcome before they can be put into practical industrial applications.

Conflicts of interest

The authors declare no conflict of interest.

Data availability

No primary research results, software or code have been included and no new data were generated or analysed as part of this review.

Acknowledgements

This work was supported by the National Natural Science Foundation (NSFC) of China (52394170–52394174) and the 10th Young Elite Scientists Sponsorship Program by CAST.

References

- 1 C. Sun, J. Liu, Y. Gong, D. P. Wilkinson and J. Zhang, *Nano Energy*, 2017, **33**, 363–386.
- 2 J. B. Goodenough and K.-S. Park, *J. Am. Chem. Soc.*, 2013, **135**, 1167–1176.
- 3 M. Liu, Z. Zeng, Y. Wu, W. Zhong, S. Lei, S. Cheng, J. Wen and J. Xie, *Energy Storage Mater.*, 2024, **65**, 103133.
- 4 Y. Wang, X. Feng, W. Huang, X. He, L. Wang and M. Ouyang, *Adv. Energy Mater.*, 2023, **13**, 2203841.
- 5 X. Feng, M. Ouyang, X. Liu, L. Lu, Y. Xia and X. He, *Energy Storage Mater.*, 2018, **10**, 246–267.
- 6 X. Liu, D. Ren, H. Hsu, X. Feng, G.-L. Xu, M. Zhuang, H. Gao, L. Lu, X. Han, Z. Chu, J. Li, X. He, K. Amine and M. Ouyang, *Joule*, 2018, **2**, 2047–2064.
- 7 X. Tang, F. Xie, Y. Lu, Z. Chen, X. Li, H. Li, X. Huang, L. Chen, Y. Pan and Y.-S. Hu, *Nano Res.*, 2023, **16**, 12579–12586.
- 8 J. Huang, K. Wu, G. Xu, M. Wu, S. Dou and C. Wu, *Chem. Soc. Rev.*, 2023, **52**, 4933–4995.
- 9 X. Tang, F. Xie, Y. Lu, H. Mao, Z. Chen, H. Pan, S. Weng, Y. Yang, X. Li, Z. Guo, Q. Guo, F. Ding, X. Hou, Y. Li, X. Wang, M.-M. Titirici, L. Chen, Y. Pan and Y.-S. Hu, *ACS Energy Lett.*, 2024, **9**, 1158–1167.
- 10 H. Pan, Y.-S. Hu and L. Chen, *Energy Environ. Sci.*, 2013, **6**, 2338–2360.
- 11 F. Li, Z. Wei, A. Manthiram, Y. Feng, J. Ma and L. Mai, *J. Mater. Chem. A*, 2019, **7**, 9406–9431.
- 12 A. Manthiram, X. Yu and S. Wang, *Nat. Rev. Mater.*, 2017, **2**, 16103.
- 13 Y.-K. Sun, *ACS Energy Lett.*, 2020, **5**, 3221–3223.
- 14 H. Huo and J. Janek, *Natl. Sci. Rev.*, 2023, **10**, nwad098.

15 Y.-S. Hu and F. Xie, *ACS Energy Lett.*, 2024, **9**, 6081–6083.

16 J. A. S. Oh, L. He, B. Chua, K. Zeng and L. Lu, *Energy Storage Mater.*, 2021, **34**, 28–44.

17 C. Zhou, S. Bag and V. Thangadurai, *ACS Energy Lett.*, 2018, **3**, 2181–2198.

18 Y.-F. Y. Yao and J. T. Kummer, *J. Inorg. Nucl. Chem.*, 1967, **29**, 2453–2475.

19 D. Lee, A. Kumar Kakarla, S. Sun, P. Joohyun Kim and J. Choi, *ChemElectroChem*, 2025, **12**, e202400612.

20 A. C. Radjendirane, D. K. Maurya, J. Ren, H. Hou, H. Algadi, B. B. Xu, Z. Guo and S. Angaiah, *Langmuir*, 2024, **40**, 16690–16712.

21 Y. Yang, S. Yang, X. Xue, X. Zhang, Q. Li, Y. Yao, X. Rui, H. Pan and Y. Yu, *Adv. Mater.*, 2024, **36**, 2308332.

22 Z. Jian, Y.-S. Hu, X. Ji and W. Chen, *Adv. Mater.*, 2017, **29**, 1601925.

23 Y. Lu, J. A. Alonso, Q. Yi, L. Lu, Z. L. Wang and C. Sun, *Adv. Energy Mater.*, 2019, **9**, 1901205.

24 H. Jia, L. Peng, C. Yu, L. Dong, S. Cheng and J. Xie, *J. Mater. Chem. A*, 2021, **9**, 5134–5148.

25 A. Hayashi, A. Sakuda and M. Tatsumisago, *Front. Energy Res.*, 2016, **4**, 25.

26 M. Jin, D. Xu, Z. Su, Z. He, X. Chen, R. Wu and Y. Guo, *ACS Energy Lett.*, 2024, **9**, 1176–1183.

27 J. Cuan, Y. Zhou, T. Zhou, S. Ling, K. Rui, Z. Guo, H. Liu and X. Yu, *Adv. Mater.*, 2019, **31**, 1803533.

28 Z. Lu, J.-X. Kang, P. Qiu and X. Chen, *Batteries Supercaps*, 2024, e202400636.

29 F. Gebert, J. Knott, R. Gorkin, S.-L. Chou and S.-X. Dou, *Energy Storage Mater.*, 2021, **36**, 10–30.

30 Y. He, S. Yang, C. Liu, Y. Ouyang, Y. Li, H. Zhu, Y. Yao, H. Yang, X. Rui and Y. Yu, *Small Methods*, 2025, 2402220.

31 C. Li and Y. Du, *ACS Nano*, 2025, **19**, 4121–4155.

32 X. Li, J. Liang, X. Yang, K. R. Adair, C. Wang, F. Zhao and X. Sun, *Energy Environ. Sci.*, 2020, **13**, 1429–1461.

33 D. C. Ginnings and T. E. Phipps, *J. Am. Chem. Soc.*, 1930, **52**, 1340–1345.

34 T. Asano, A. Sakai, S. Ouchi, M. Sakaida, A. Miyazaki and S. Hasegawa, *Adv. Mater.*, 2018, **30**, 1803075.

35 X. Li, J. Liang, N. Chen, J. Luo, K. R. Adair, C. Wang, M. N. Banis, T.-K. Sham, L. Zhang, S. Zhao, S. Lu, H. Huang, R. Li and X. Sun, *Angew. Chem., Int. Ed.*, 2019, **58**, 16427–16432.

36 K. Wang, Q. Ren, Z. Gu, C. Duan, J. Wang, F. Zhu, Y. Fu, J. Hao, J. Zhu, L. He, C.-W. Wang, Y. Lu, J. Ma and C. Ma, *Nat. Commun.*, 2021, **12**, 4410.

37 S. Zhang, F. Zhao, J. Chen, J. Fu, J. Luo, S. H. Alahakoon, L.-Y. Chang, R. Feng, M. Shakouri, J. Liang, Y. Zhao, X. Li, L. He, Y. Huang, T.-K. Sham and X. Sun, *Nat. Commun.*, 2023, **14**, 3780.

38 Y. Tanaka, K. Ueno, K. Mizuno, K. Takeuchi, T. Asano and A. Sakai, *Angew. Chem., Int. Ed.*, 2023, **62**, e202217581.

39 T. Dai, S. Wu, Y. Lu, Y. Yang, Y. Liu, C. Chang, X. Rong, R. Xiao, J. Zhao, Y. Liu, W. Wang, L. Chen and Y.-S. Hu, *Nat. Energy*, 2023, **8**, 1221–1228.

40 H. Kwak, J. Lyoo, J. Park, Y. Han, R. Asakura, A. Remhof, C. Battaglia, H. Kim, S.-T. Hong and Y. S. Jung, *Energy Storage Mater.*, 2021, **37**, 47–54.

41 Y. Hu, J. Fu, J. Xu, J. Luo, F. Zhao, H. Su, Y. Liu, X. Lin, W. Li, J. T. Kim, X. Hao, X. Yao, Y. Sun, J. Ma, H. Ren, M. Yang, Y. Huang and X. Sun, *Matter*, 2024, **7**, 1018–1034.

42 E. A. Wu, S. Banerjee, H. Tang, P. M. Richardson, J.-M. Doux, J. Qi, Z. Zhu, A. Grenier, Y. Li, E. Zhao, G. Deysher, E. Sebti, H. Nguyen, R. Stephens, G. Verbist, K. W. Chapman, R. J. Clément, A. Banerjee, Y. S. Meng and S. P. Ong, *Nat. Commun.*, 2021, **12**, 1256.

43 R. Schlem, A. Banik, M. Eckardt, M. Zobel and W. G. Zeier, *ACS Appl. Energy Mater.*, 2020, **3**, 10164–10173.

44 L. Zhou, J. D. Bazak, C. Li and L. F. Nazar, *ACS Energy Lett.*, 2024, **9**, 4093–4101.

45 A. Bohnsack, G. Balzer, H.-U. Güdel, M. S. Wickleder and G. Meyer, *Z. für Anorg. Allg. Chem.*, 1997, **623**, 1352–1356.

46 A. Bohnsack, F. Stenzel, A. Zajonc, G. Balzer, M. S. Wickleder and G. Meyer, *Z. für Anorg. Allg. Chem.*, 1997, **623**, 1067–1073.

47 Y. Sun, G. Bian, W. Tao, C. Zhai, M. Zhong and Z. Qiao, *Calphad*, 2012, **39**, 1–10.

48 X. Meng, Y. Sun, S. Yuan, Z. Ma, Y. Wang and Z. Qiao, *Calphad*, 2006, **30**, 301–307.

49 P. Ridley, L. H. B. Nguyen, E. Sebti, B. Han, G. Duong, Y.-T. Chen, B. Sayahpour, A. Cronk, G. Deysher, S.-Y. Ham, J. A. S. Oh, E. A. Wu, D. H. S. Tan, J.-M. Doux, R. Clément, J. Jang and Y. S. Meng, *Matter*, 2024, **7**, 485–499.

50 S. Zhang, F. Zhao, L.-Y. Chang, Y.-C. Chuang, Z. Zhang, Y. Zhu, X. Hao, J. Fu, J. Chen, J. Luo, M. Li, Y. Gao, Y. Huang, T.-K. Sham, M. D. Gu, Y. Zhang, G. King and X. Sun, *J. Am. Chem. Soc.*, 2024, **146**, 2977–2985.

51 S. Muy, J. Voss, R. Schlem, R. Koerver, S. J. Sedlmaier, F. Maglia, P. Lamp, W. G. Zeier and Y. Shao-Horn, *iScience*, 2019, **16**, 270–282.

52 C. Wang, J. Liang, J. Luo, J. Liu, X. Li, F. Zhao, R. Li, H. Huang, S. Zhao, L. Zhang, J. Wang and X. Sun, *Sci. Adv.*, 2021, **7**, eabhb1896.

53 Q. Wang, Y. Zhou, X. Wang, H. Guo, S. Gong, Z. Yao, F. Wu, J. Wang, S. Ganapathy, X. Bai, B. Li, C. Zhao, J. Janek and M. Wagemaker, *Nat. Commun.*, 2024, **15**, 1050.

54 P. Kuske, W. Schäfer and H. D. Lutz, *Mater. Res. Bull.*, 1988, **23**, 1805–1808.

55 Z. Wei, L. F. Nazar and J. Janek, *Batteries Supercaps*, 2024, **7**, e202400005.

56 H. D. Lutz, P. Kuske and K. Wussow, *Z. für Anorg. Allg. Chem.*, 1987, **553**, 172–178.

57 M. Schneider, P. Kuske and H. D. Lutz, *Z. Naturforsch. B*, 1993, **48**, 1–6.

58 R. Kanno, Y. Takeda, K. Murata and O. Yamamoto, *Solid State Ionics*, 1990, **39**, 233–244.

59 X. Li, J. Liang, K. R. Adair, J. Li, W. Li, F. Zhao, Y. Hu, T.-K. Sham, L. Zhang, S. Zhao, S. Lu, H. Huang, R. Li, N. Chen and X. Sun, *Nano Lett.*, 2020, **20**, 4384–4392.



60 J. Fu, S. Wang, J. Liang, S. H. Alahakoon, D. Wu, J. Luo, H. Duan, S. Zhang, F. Zhao, W. Li, M. Li, X. Hao, X. Li, J. Chen, N. Chen, G. King, L.-Y. Chang, R. Li, Y. Huang, M. Gu, T.-K. Sham, Y. Mo and X. Sun, *J. Am. Chem. Soc.*, 2023, **145**, 2183–2194.

61 J. Liang, X. Li, S. Wang, K. R. Adair, W. Li, Y. Zhao, C. Wang, Y. Hu, L. Zhang, S. Zhao, S. Lu, H. Huang, R. Li, Y. Mo and X. Sun, *J. Am. Chem. Soc.*, 2020, **142**, 7012–7022.

62 Z. Xu, X. Chen, K. Liu, R. Chen, X. Zeng and H. Zhu, *Chem. Mater.*, 2019, **31**, 7425–7433.

63 R. Schlem, T. Bernges, C. Li, M. A. Kraft, N. Minafra and W. G. Zeier, *ACS Appl. Energy Mater.*, 2020, **3**, 3684–3691.

64 X. Li, J. T. Kim, J. Luo, C. Zhao, Y. Xu, T. Mei, R. Li, J. Liang and X. Sun, *Nat. Commun.*, 2024, **15**, 53.

65 F. Stenzel and G. Meyer, *Z. fur Anorg. Allg. Chem.*, 1993, **619**, 652–660.

66 H. D. Lutz, W. Schmidt and H. Haeuseler, *J. Phys. Chem. Solids*, 1981, **42**, 287–289.

67 R. Kanno, Y. Takeda, K. Takada and O. Yamamoto, *J. Electrochem. Soc.*, 1984, **131**, 469.

68 C. J. J. Van Loon and J. De Jong, *Acta Crystallogr., Sect. B*, 1975, **31**, 2549–2550.

69 L. Zhou, C. Y. Kwok, A. Shyamsunder, Q. Zhang, X. Wu and L. F. Nazar, *Energy Environ. Sci.*, 2020, **13**, 2056–2063.

70 J. Liang, E. van der Maas, J. Luo, X. Li, N. Chen, K. R. Adair, W. Li, J. Li, Y. Hu, J. Liu, L. Zhang, S. Zhao, S. Lu, J. Wang, H. Huang, W. Zhao, S. Parnell, R. I. Smith, S. Ganapathy, M. Wagemaker and X. Sun, *Adv. Energy Mater.*, 2022, **12**, 2103921.

71 Y.-C. Yin, J.-T. Yang, J.-D. Luo, G.-X. Lu, Z. Huang, J.-P. Wang, P. Li, F. Li, Y.-C. Wu, T. Tian, Y.-F. Meng, H.-S. Mo, Y.-H. Song, J.-N. Yang, L.-Z. Feng, T. Ma, W. Wen, K. Gong, L.-J. Wang, H.-X. Ju, Y. Xiao, Z. Li, X. Tao and H.-B. Yao, *Nature*, 2023, **616**, 77–83.

72 R. Schlem, S. Muy, N. Prinz, A. Banik, Y. Shao-Horn, M. Zobel and W. G. Zeier, *Adv. Energy Mater.*, 2020, **10**, 1903719.

73 S. Y. Kim, K. Kaup, K.-H. Park, A. Assoud, L. Zhou, J. Liu, X. Wu and L. F. Nazar, *ACS Mater. Lett.*, 2021, **3**, 930–938.

74 K. Yamada, K. Kumano and T. Okuda, *Solid State Ionics*, 2005, **176**, 823–829.

75 S. Wang, Q. Bai, A. M. Nolan, Y. Liu, S. Gong, Q. Sun and Y. Mo, *Angew. Chem., Int. Ed.*, 2019, **58**, 8039–8043.

76 F. Lissner, K. Krämer, T. Schleid, G. Meyer, Z. Hu and G. Kaindl, *Z. fur Anorg. Allg. Chem.*, 1994, **620**, 444–450.

77 C. Fu, Y. Li, W. Xu, X. Feng, W. Gu, J. Liu, W. Deng, W. Wang, A. M. M. Abeykoon, L. Su, L. Zhu, X. Wu and H. Xiang, *Nat. Commun.*, 2024, **15**, 4315.

78 J. Fu, S. Wang, D. Wu, J. Luo, C. Wang, J. Liang, X. Lin, Y. Hu, S. Zhang, F. Zhao, W. Li, M. Li, H. Duan, Y. Zhao, M. Gu, T.-K. Sham, Y. Mo and X. Sun, *Adv. Mater.*, 2024, **36**, 2308012.

79 F. Li, X. Cheng, G. Lu, Y.-C. Yin, Y.-C. Wu, R. Pan, J.-D. Luo, F. Huang, L.-Z. Feng, L.-L. Lu, T. Ma, L. Zheng, S. Jiao, R. Cao, Z.-P. Liu, H. Zhou, X. Tao, C. Shang and H.-B. Yao, *J. Am. Chem. Soc.*, 2023, **145**, 27774–27787.

80 X. Lin, S. Zhang, M. Yang, B. Xiao, Y. Zhao, J. Luo, J. Fu, C. Wang, X. Li, W. Li, F. Yang, H. Duan, J. Liang, B. Fu, H. Abdolvand, J. Guo, G. King and X. Sun, *Nat. Mater.*, 2025, **24**, 83–91.

81 R. Xu, J. Yao, Z. Zhang, L. Li, Z. Wang, D. Song, X. Yan, C. Yu and L. Zhang, *Adv. Sci.*, 2022, **9**, 2204633.

82 S.-K. Jung, H. Gwon, G. Yoon, L. J. Miara, V. Lacivita and J.-S. Kim, *ACS Energy Lett.*, 2021, **6**, 2006–2015.

83 S. V. Patel, V. Lacivita, H. Liu, E. Truong, Y. Jin, E. Wang, L. Miara, R. Kim, H. Gwon, R. Zhang, I. Hung, Z. Gan, S.-K. Jung and Y.-Y. Hu, *Sci. Adv.*, 2023, **9**, eadj9930.

84 X. Yang, S. Gupta, Y. Chen, D. Sari, H.-M. Hau, Z. Cai, C. Dun, M. Qi, L. Ma, Y. Liu, J. J. Urban and G. Ceder, *Adv. Energy Mater.*, 2024, **14**, 2400163.

85 K.-H. Park, K. Kaup, A. Assoud, Q. Zhang, X. Wu and L. F. Nazar, *ACS Energy Lett.*, 2020, **5**, 533–539.

86 Y. Liu, S. Wang, A. M. Nolan, C. Ling and Y. Mo, *Adv. Energy Mater.*, 2020, **10**, 2002356.

87 T. H. Wan and F. Ciucci, *ACS Appl. Energy Mater.*, 2021, **4**, 7930–7941.

88 L. Zhou, T.-T. Zuo, C. Y. Kwok, S. Y. Kim, A. Assoud, Q. Zhang, J. Janek and L. F. Nazar, *Nat. Energy*, 2022, **7**, 83–93.

89 J. Wu, J. Li and X. Yao, *Adv. Funct. Mater.*, 2025, **35**, 2416671.

90 J. Park, D. Han, H. Kwak, Y. Han, Y. J. Choi, K.-W. Nam and Y. S. Jung, *Chem. Eng. J.*, 2021, **425**, 130630.

91 H. Kwak, D. Han, J. P. Son, J. S. Kim, J. Park, K.-W. Nam, H. Kim and Y. S. Jung, *Chem. Eng. J.*, 2022, **437**, 135413.

92 H. Kwak, D. Han, J. Lyoo, J. Park, S. H. Jung, Y. Han, G. Kwon, H. Kim, S.-T. Hong, K.-W. Nam and Y. S. Jung, *Adv. Energy Mater.*, 2021, **11**, 2003190.

93 Y. Tomita, H. Matsushita, K. Kobayashi, Y. Maeda and K. Yamada, *Solid State Ionics*, 2008, **179**, 867–870.

94 Z. Liu, S. Ma, J. Liu, S. Xiong, Y. Ma and H. Chen, *ACS Energy Lett.*, 2021, **6**, 298–304.

95 Z. Liu, P.-H. Chien, S. Wang, S. Song, M. Lu, S. Chen, S. Xia, J. Liu, Y. Mo and H. Chen, *Nat. Chem.*, 2024, **16**, 1584–1591.

96 M. A. Plass, S. Bette, R. E. Dinnebier and B. V. Lotsch, *Chem. Mater.*, 2022, **34**, 3227–3235.

97 S. Yu, K. Kim, B. C. Wood, H.-G. Jung and K. Y. Chung, *J. Mater. Chem. A*, 2022, **10**, 24301–24309.

98 E. Umeshbabu, S. Maddukuri, Y. Hu, M. Fichtner and A. R. Munnangi, *ACS Appl. Mater. Interfaces*, 2022, **14**, 25448–25456.

99 X. Luo, X. He, H. Su, Y. Zhong, X. Wang and J. Tu, *Chem. Eng. J.*, 2023, **465**, 143036.

100 S. Zhang, F. Zhao, S. Wang, J. Liang, J. Wang, C. Wang, H. Zhang, K. Adair, W. Li, M. Li, H. Duan, Y. Zhao, R. Yu, R. Li, H. Huang, L. Zhang, S. Zhao, S. Lu, T.-K. Sham, Y. Mo and X. Sun, *Adv. Energy Mater.*, 2021, **11**, 2100836.

101 H. Kwak, J.-S. Kim, D. Han, J. S. Kim, J. Park, G. Kwon, S.-M. Bak, U. Heo, C. Park, H.-W. Lee, K.-W. Nam, D.-H. Seo and Y. S. Jung, *Nat. Commun.*, 2023, **14**, 2459.

102 J. Wang, F. Chen, L. Hu and C. Ma, *Nano Lett.*, 2023, **23**, 6081–6087.



103 B. Li, Y. Li, H.-S. Zhang, T.-T. Wu, S. Guo and A.-M. Cao, *Sci. China Mater.*, 2023, **66**, 3123–3128.

104 K.-H. Park, S. Y. Kim, M. Jung, S.-B. Lee, M.-J. Kim, I.-J. Yang, J.-H. Hwang, W. Cho, G. Chen, K. Kim and J. Yu, *ACS Appl. Mater. Interfaces*, 2023, **15**, 58367–58376.

105 B. Hong, L. Gao, C. Li, G. Lai, J. Zhu, D. Huang, Y. Zuo, W. Yin, M. Sun, S. Zhao, J. Zheng, S. Han and R. Zou, *Nat. Commun.*, 2025, **16**, 143.

106 B. Hong, L. Gao, P. Nan, Y. Li, M. Liu, R. Zou, J. Gu, Q. Xu, J. Zhu and S. Han, *Angew. Chem., Int. Ed.*, 2025, **64**, e202415847.

107 Z. Song, T. Wang, H. Yang, W. H. Kan, Y. Chen, Q. Yu, L. Wang, Y. Zhang, Y. Dai, H. Chen, W. Yin, T. Honda, M. Avdeev, H. Xu, J. Ma, Y. Huang and W. Luo, *Nat. Commun.*, 2024, **15**, 1481.

108 X. Sun, *Sci. Bull.*, 2023, **68**, 2682–2683.

109 W. Wang, *Mater. Futures*, 2023, **2**, 047502.

110 Y. Ren and C.-W. Nan, *J. Materomics*, 2024, **10**, 707–708.

111 S. Zhang, Y. Xu, H. Wu, T. Pang, N. Zhang, C. Zhao, J. Yue, J. Fu, S. Xia, X. Zhu, G. Wang, H. Duan, B. Xiao, T. Mei, J. Liang, X. Sun and X. Li, *Angew. Chem., Int. Ed.*, 2024, **63**, e202401373.

112 G. Wang, S. Zhang, H. Wu, M. Zheng, C. Zhao, J. Liang, L. Zhou, J. Yue, X. Zhu, Y. Xu, N. Zhang, T. Pang, J. Fu, W. Li, Y. Xia, W. Yin, X. Sun and X. Li, *Adv. Mater.*, 2025, **37**, 2410402.

113 H. Duan, C. Wang, X.-S. Zhang, J. Fu, W. Li, J. Wan, R. Yu, M. Fan, F. Ren, S. Wang, M. Zheng, X. Li, J. Liang, R. Wen, S. Xin, Y.-G. Guo and X. Sun, *J. Am. Chem. Soc.*, 2024, **146**, 29335–29343.

114 I. You, B. Singh, M. Cui, G. Goward, L. Qian, Z. Arthur, G. King and L. F. Nazar, *Energy Environ. Sci.*, 2025, **18**, 478–491.

115 L. Shen, J.-L. Li, W.-J. Kong, C.-X. Bi, P. Xu, X.-Y. Huang, W.-Z. Huang, F. Fu, Y.-C. Le, C.-Z. Zhao, H. Yuan, J.-Q. Huang and Q. Zhang, *Adv. Funct. Mater.*, 2024, **34**, 2408571.

116 X. Lin, Y. Zhao, C. Wang, J. Luo, J. Fu, B. Xiao, Y. Gao, W. Li, S. Zhang, J. Xu, F. Yang, X. Hao, H. Duan, Y. Sun, J. Guo, Y. Huang and X. Sun, *Angew. Chem., Int. Ed.*, 2024, **63**, e202314181.

117 D. Li, D. Yu, G. Zhang, A. Du, Z. Ye, Y. Jia, W. Hou, T. Xu, F. Li, S. Chi, Y. Zhu and C. Yang, *Angew. Chem., Int. Ed.*, 2025, **64**, e202419735.

118 W. Li, J. Liang, M. Li, K. R. Adair, X. Li, Y. Hu, Q. Xiao, R. Feng, R. Li, L. Zhang, S. Lu, H. Huang, S. Zhao, T.-K. Sham and X. Sun, *Chem. Mater.*, 2020, **32**, 7019–7027.

119 Y. Zhu and Y. Mo, *Angew. Chem., Int. Ed.*, 2020, **59**, 17472–17476.

120 S. Wang, X. Xu, C. Cui, C. Zeng, J. Liang, J. Fu, R. Zhang, T. Zhai and H. Li, *Adv. Funct. Mater.*, 2022, **32**, 2108805.

121 R. L. Sacci, T. H. Bennett, A. R. Drews, V. Anandan, M. J. Kirkham, L. L. Daemen and J. Nanda, *J. Mater. Chem. A*, 2021, **9**, 990–996.

122 Y. Qie, S. Wang, S. Fu, H. Xie, Q. Sun and P. Jena, *J. Phys. Chem. Lett.*, 2020, **11**, 3376–3383.

123 G. H. Chun, J. H. Shim and S. Yu, *ACS Appl. Mater. Interfaces*, 2022, **14**, 1241–1248.

124 S. Wenzel, T. Leichtweiss, D. Krüger, J. Sann and J. Janek, *Solid State Ionics*, 2015, **278**, 98–105.

125 D. Park, H. Park, Y. Lee, S.-O. Kim, H.-G. Jung, K. Y. Chung, J. H. Shim and S. Yu, *ACS Appl. Mater. Interfaces*, 2020, **12**, 34806–34814.

126 G. Xu, L. Luo, J. Liang, S. Zhao, R. Yang, C. Wang, T. Yu, L. Wang, W. Xiao, J. Wang, J. Yu and X. Sun, *Nano Energy*, 2022, **92**, 106674.

127 Y. Han, S. H. Jung, H. Kwak, S. Jun, H. H. Kwak, J. H. Lee, S.-T. Hong and Y. S. Jung, *Adv. Energy Mater.*, 2021, **11**, 2100126.

128 S. H. Jung, U.-H. Kim, J.-H. Kim, S. Jun, C. S. Yoon, Y. S. Jung and Y.-K. Sun, *Adv. Energy Mater.*, 2020, **10**, 1903360.

129 F. Zhao, S. Zhang, S. Wang, C. M. Andrei, H. Yuan, J. Zhou, J. Wang, Z. Zhuo, Y. Zhong, H. Su, J. T. Kim, R. Yu, Y. Gao, J. Guo, T.-K. Sham, Y. Mo and X. Sun, *Energy Environ. Sci.*, 2024, **17**, 4055–4063.

130 Y. Fu and C. Ma, *Sci. China Mater.*, 2021, **64**, 1378–1385.

131 L. M. Rieger, R. Schlem, J. Sann, W. G. Zeier and J. Janek, *Angew. Chem., Int. Ed.*, 2021, **60**, 6718–6723.

132 W. Li, M. Li, S. Wang, P.-H. Chien, J. Luo, J. Fu, X. Lin, G. King, R. Feng, J. Wang, J. Zhou, R. Li, J. Liu, Y. Mo, T.-K. Sham and X. Sun, *Nat. Nanotechnol.*, 2025, **20**, 265–275.

133 W. Li, M. Li, P.-H. Chien, S. Wang, C. Yu, G. King, Y. Hu, Q. Xiao, M. Shakouri, R. Feng, B. Fu, H. Abdolvand, A. Fraser, R. Li, Y. Huang, J. Liu, Y. Mo, T.-K. Sham and X. Sun, *Sci. Adv.*, 2023, **9**, eadh4626.

134 B. Ma, R. Li, H. Zhu, T. Zhou, L. Lv, H. Zhang, S. Zhang, L. Chen, J. Wang, X. Xiao, T. Deng, L. Chen, C. Wang and X. Fan, *Adv. Mater.*, 2024, **36**, 2402324.

135 S. Zhang, F. Zhao, H. Su, Y. Zhong, J. Liang, J. Chen, M. L. Zheng, J. Liu, L.-Y. Chang, J. Fu, S. H. Alahakoon, Y. Hu, Y. Liu, Y. Huang, J. Tu, T.-K. Sham and X. Sun, *Angew. Chem., Int. Ed.*, 2024, **63**, e202316360.

136 H. Zhang, F. Xu, X. Chen and W. Xia, *Batteries*, 2023, **9**, 510.

137 H. Wu, J. Qu, X. Yan, S. Zhang, X. Wang, J. Liang, N. Zhang, B. Dai, J. Yue, T. Pang, T. Mei, Y. Luo, H. Lai, X. Wang, L. Zhou, S. Wang, X. Sun and X. Li, *Adv. Mater.*, 2025, 2502067.

138 Y. Li, Q. Liu, S. Wu, L. Geng, J. Popovic, Y. Li, Z. Chen, H. Wang, Y. Wang and T. Dai, *J. Am. Chem. Soc.*, 2023, **145**, 10576–10583.

139 Z. Li, Y. Mu, K. Lü, G. Kang, T. Yang, S. Huang, M. Wei, L. Zeng and Y. Li, *Angew. Chem., Int. Ed.*, 2025, **64**, e202501749.

140 Y. Wu, L. Wang, S. Wei, X. Bi, H. Zhuo, W. Xiao, T. Yu, Y. Duan, C. Zhao, R. Yang, J. Liang, X. Li, J. Wang and X. Sun, *Adv. Energy Mater.*, 2024, **14**, 2401528.

141 L. Zhou, S. Zhang, W. Li, B. Li, N. S. Grundish, P. Ren, X. Wang, N. Wu, W. Zhou and Y. Li, *J. Am. Chem. Soc.*, 2025, **147**, 15136–15145.

